A&A, 697, A15 (2025)
https://doi.org/10.1051/0004-6361/202450776
© The Authors 2025

Euclid on Sky

Astronomy & Astrophysics
Special issue

Euclid: Early Release Observations – A preview of the *Euclid* era through a galaxy cluster magnifying lens[★]

H. Atek[1,★★], R. Gavazzi[2,1], J. R. Weaver[3], J. M. Diego[4], T. Schrabback[5], N. A. Hatch[6], N. Aghanim[7], H. Dole[7], W. G. Hartley[8], S. Taamoli[9], G. Congedo[10], Y. Jimenez-Teja[11,12], J.-C. Cuillandre[13], E. Bañados[14], S. Belladitta[14,15], R. A. A. Bowler[16], M. Franco[17], M. Jauzac[18,19,20,21], G. Mahler[22,18,19], J. Richard[23], P.-F. Rocci[7], S. Serjeant[24], S. Toft[34,25], D. Abriola[26], P. Bergamini[26,15], A. Biviano[27,28], P. Dimauro[29,12], M. Ezziati[2], J. B. Golden-Marx[6], C. Grillo[26,30], A. C. N. Hughes[31], Y. Kang[8], J.-P. Kneib[32], M. Lombardi[26], G. A. Mamon[1,33], C. J. R. McPartland[34,25], M. Meneghetti[15,35], H. Miyatake[36,37,38], M. Montes[39,40], D. J. Mortlock[31,41], P. A. Oesch[8,25,34], N. Okabe[42,43,44], P. Rosati[45,15], A. N. Taylor[10], F. Tarsitano[8], J. Weller[46,47], M. Kluge[47], R. Laureijs[48], S. Paltani[8], T. Saifollahi[49,50], M. Schirmer[14], C. Stone[51], A. Mora[52], B. Altieri[53], A. Amara[54], S. Andreon[55], N. Auricchio[15], M. Baldi[56,15,35], A. Balestra[57], S. Bardelli[15], A. Basset[58], R. Bender[47,46], C. Bodendorf[47], D. Bonino[59], E. Branchini[60,61,55], M. Brescia[62,63,64], J. Brinchmann[65,66], S. Camera[67,68,59], G. P. Candini[69], V. Capobianco[59], C. Carbone[30], V. F. Cardone[29,70], J. Carretero[71,72], S. Casas[73], F. J. Castander[74,75], M. Castellano[29], S. Cavuoti[63,64], A. Cimatti[76], C. J. Conselice[16], L. Conversi[77,53], Y. Copin[78], L. Corcione[59], F. Courbin[32], H. M. Courtois[79], A. Da Silva[80,81], H. Degaudenzi[8], A. M. Di Giorgio[82], J. Dinis[80,81], M. Douspis[7], F. Dubath[8], X. Dupac[53], S. Dusini[83], A. Ealet[78], M. Farina[82], S. Farrens[13], S. Ferriol[78], S. Fotopoulou[84], M. Frailis[27], E. Franceschi[15], S. Galeotta[27], W. Gillard[85], B. Gillis[10], C. Giocoli[15,86], P. Gómez-Alvarez[87,53], A. Grazian[57], F. Grupp[47,46], L. Guzzo[26,55], M. Hailey[69], S. V. H. Haugan[88], J. Hoar[53], H. Hoekstra[89], M. S. Holliman[10], W. Holmes[90], I. Hook[91], F. Hormuth[92], A. Hornstrup[93,34], P. Hudelot[1], K. Jahnke[14], M. Jhabvala[94], E. Keihänen[95], S. Kermiche[85], A. Kiessling[90], T. Kitching[69], R. Kohley[53], B. Kubik[78], K. Kuijken[89], M. Kümmel[46], M. Kunz[96], H. Kurki-Suonio[97,98], O. Lahav[99], D. Le Mignant[2], S. Ligori[59], P. B. Lilje[88], V. Lindholm[97,98], I. Lloro[100], D. Maino[26,30,101], E. Maiorano[15], O. Mansutti[27], O. Marggraf[102], K. Markovic[90], N. Martinet[2], F. Marulli[103,15,35], R. Massey[18,19], S. Maurogordato[104], H. J. McCracken[1], S. Mei[105], Y. Mellier[33,1], E. Merlin[29], G. Meylan[32], M. Moresco[103,15], L. Moscardini[103,15,35], R. Nakajima[102], R. C. Nichol[54], S.-M. Niemi[48], C. Padilla[106], K. Paech[47], F. Pasian[27], J. A. Peacock[10], K. Pedersen[107], W. J. Percival[108,109,110], V. Pettorino[48], S. Pires[13], G. Polenta[111], M. Poncet[58], L. A. Popa[112], L. Pozzetti[15], F. Raison[47], A. Renzi[113,83], J. Rhodes[90], G. Riccio[63], E. Romelli[27], M. Roncarelli[15], R. Saglia[46,47], D. Sapone[114], P. Schneider[102], A. Secroun[85], G. Seidel[14], S. Serrano[75,115,74], C. Sirignano[113,83], G. Sirri[35], J. Skottfelt[116], L. Stanco[83], P. Tallada-Crespí[71,72], H. I. Teplitz[117], I. Tereno[80,118], R. Toledo-Moreo[119], I. Tutusaus[120], L. Valenziano[15,121], T. Vassallo[46,27], G. Verdoes Kleijn[50], A. Veropalumbo[55,61,122], Y. Wang[117], E. Zucca[15], C. Baccigalupi[28,27,123,124], C. Burigana[125,121], G. Castignani[15], Z. Sakr[126,120,127], V. Scottez[33,128], M. Viel[28,27,124,123,129], P. Simon[102], D. Stern[90], J. Martín-Fleitas[52], and D. Scott[130]

(Affiliations can be found after the references)

Received 18 May 2024 / Accepted 17 June 2024

ABSTRACT

We present the first analysis of the *Euclid* Early Release Observations (ERO) program that targets fields around two lensing clusters, Abell 2390 and Abell 2764. We use imaging data from the Visible instrument (VIS) and the Near-Infrared Spectrometer and Photometer (NISP) to produce photometric catalogs for a total of ~500 000 objects. The imaging data reach a typical depth of 5 σ in the range 25.1–25.4 AB in the NISP bands and 27.1–27.3 AB in the VIS band. Using the Lyman-break method in combination with photometric redshifts, we searched for high-redshift galaxies. We identified 30 Lyman-break galaxy (LBG) candidates at $z > 6$ and 139 extremely red sources (ERSs), most of which likely lie at lower redshift. The VIS imaging is deeper than the NISP imaging, which means that we can routinely identify high-redshift Lyman-break galaxies at about a magnitude of 3, which reduces contamination by brown dwarf stars and low-redshift galaxies. The difficulty of spatially resolving most of these sources in $0\farcs3$ pix^{-1} imaging means that it is difficult to distinguish between galaxies and quasars. Spectroscopic follow-up campaigns of these bright sources will help us to constrain the

---

[★] This paper is published on behalf of the Euclid Consortium.

[★★] Corresponding author; `atek@iap.fr`

bright end of the ultraviolet galaxy luminosity function and the quasar luminosity function at $z > 6$, and it will constrain the physical nature of these objects. Additionally, we performed a combined strong- and weak-lensing analysis of A2390, and we show that *Euclid* will contribute to constraining the virial mass of galaxy clusters better. We also identify optical and near-infrared counterparts of known $z > 0.6$ clusters in these data. These counterparts exhibit strong-lensing features. This establishes that *Euclid* can characterize high-redshift clusters. Finally, we provide a glimpse of the ability of *Euclid* to map the intracluster light out to larger radii than current facilities, which enables us to understand the cluster assembly history better and to map the dark matter distribution. This initial dataset illustrates the diverse spectrum of legacy science that is possible with the *Euclid* survey.

Key words. galaxies: clusters: general – galaxies: high-redshift – cosmology: observations

1. Introduction

Beyond its primary cosmology science goals, the *Euclid* mission will provide a sample of more than 200 000 high-redshift galaxies across 14 000 $\deg^2$ of the extragalactic sky (Euclid Collaboration: Scaramella et al. 2022; Euclid Collaboration: Mellier et al. 2025). This will enable a wide array of legacy science. In particular, the near-infrared (NIR) capabilities of the Near-Infrared Spectrometer and Photometer (NISP) instrument (Euclid Collaboration: Jahnke et al. 2025) and the wide optical coverage of the Visible instrument (VIS; Euclid Collaboration: Cropper et al. 2025) allow us to detect star-forming galaxies and quasars during the epoch of reionization. This epoch lasted from $z = 6$ to $z = 9$. The deep survey component of *Euclid* will map a total of 53 $\deg^2$, that is, in the Euclid deep field north (EDF-N), the Euclid deep field south (EDF-S), and the Euclid deep field Fornax (EDF-F), down to a $5\,\sigma$ point-source limiting magnitude of ~27.7 in the NIR and 29.4 in the visible (Euclid Collaboration: Mellier et al. 2025). In comparison, the widest areas covered by the *Hubble* Space Telescope (HST) and the JWST, are about 1 $\deg^2$. The wide survey will reach a $5\,\sigma$ magnitude depth of 26.2 in VIS/I_E and 24.0 in all NISP bands. The sky coverage is optimized for maximum overlap with ground-based ancillary data. These data greatly help us to estimate the photometric redshift (Euclid Collaboration: van Mierlo et al. 2022; Euclid Collaboration: Scaramella et al. 2022; Euclid Collaboration: Mellier et al. 2025).

One of the main legacy science components is the identification of distant galaxies and quasars at redshifts greater than 6. This will primarily rely on the detection of the Lyman break in the VIS I_E filter at $z \sim 7$ and in one of the NISP filters at higher redshifts. Based on the current survey design, more than 10 000 galaxies are expected at $z \sim 7$ and up to 2000 galaxies at $z \sim 8$, assuming a Schechter UV luminosity function (Bouwens et al. 2015). Over 100 quasars are expected over $7.0 < z < 7.5$, and about 25 quasars beyond $z = 7.5$, assuming a declining quasar luminosity function beyond $z = 6$ (Euclid Collaboration: Barnett et al. 2019). The brightness of these sources, $J_\mathrm{E} \gtrsim 21$ opens up spectroscopic follow-up opportunities with ground-based telescopes to robustly determine the bright end of the galaxy and the quasar luminosity functions. In addition, *Euclid* will observe hundreds of lensing clusters, enabling the detection of magnified galaxies and quasars at $z > 6$.

We present an overview and early results of the Early Release Observations (ERO) program Magnifying Lens here, which targets two cluster fields, Abell 2390 and Abell 2764 (hereafter, A2390 and A2764, respectively). This program represents a unique opportunity to showcase the science questions that *Euclid* observations of galaxy clusters will be able to address. This paper serves as an introduction to these initial measurements and findings in the cluster and blank fields. Specifically, it illustrates how *Euclid* will identify high-redshift dropout sources both in blank regions and behind lensing clusters. A companion paper is dedicated to the search for high-redshift candidates at $z > 6$ (see Weaver et al. 2025). We also take this opportunity to investigate the challenges in robustly identifying high-redshift objects and the potentially contaminating sources. These observations also offer a glimpse into the combination of strong- and weak-lensing analyses to map the mass distribution in the lensing clusters that will be uncovered in *Euclid*, data. Furthermore, *Euclid* offers a wide field of view, which is necessary to map the intracluster light in the outer regions of the cluster.

The paper is organized as follows. In Sect. 2, we describe the ERO program and the characteristics of the targets. Section 3 is dedicated to the observations and data reduction of the VIS and NISP imaging. The photometric catalogs that are released with this publication are described in Sect. 4. In terms of the scientific exploitation of this dataset, we present the VIS-dropout sources in Sect. 5, the weak-lensing analysis of A2390 in Sect. 6, and a combined strong- and weak-lensing analysis of A2390 in Sect. 7. The search for high-redshift galaxy clusters is discussed in Sect. 8, while the study of the intracluster light in A2390 is presented in Sect. 9. A summary of this work is presented in Sect. 10. We assumed a flat ΛCDM cosmology with $H_0 = 70\,\mathrm{km\,s^{-1}\,Mpc^{-1}}$, $\Omega_\mathrm{m} = 0.3$, and $\Omega_\Lambda = 0.7$. All magnitudes are in the AB system.

2. The ERO program

The ERO program was designed to obtain a comprehensive dataset spanning multiple interdisciplinary working groups, including but not limited to the groups focused on the primordial universe, galaxy evolution, and active galactic nuclei (AGN), strong and weak lensing, and galaxy cluster physics. These observations provide a first glimpse of the *Euclid* imaging data, with the aim of facilitating the inaugural evaluation of tools, data quality, and methods developed over the preceding decade. The early investigation of the dataset will help us to reveal and address the challenges and limitations for a full scientific exploitation of the prime mission survey data.

The ERO observations for this project were taken on 28 November 2023 as part of the performance-verification (PV) phase of the *Euclid* mission.

2.1. Abell 2390

The first ERO target was the galaxy cluster A2390, RA=$21^\mathrm{h}53^\mathrm{m}35.50^\mathrm{s}$, Dec=$17°41'41.54''$, located at a redshift of $z = 0.228$ (Sohn et al. 2020). It is one of the richest clusters in the Abell catalog (Pello et al. 1991; Le Borgne et al. 1991; Feix et al. 2010), with an estimated mass M_{200}[1] ranging from $1.53 \times 10^{15}\,M_\odot$ from weak lensing (Okabe & Smith 2016) to $1.84 \times 10^{15}\,M_\odot$ from the projected phase-space of galaxies (Sohn et al. 2020). It includes multiple well-studied lensing arcs (e.g., Olmstead et al. 2014; Richard et al. 2021). It also displays bright X-ray emission with a luminosity of $2.7 \times 10^{45}\,\mathrm{erg\,s^{-1}}$ in the 0.1–2.4 keV range (Boehringer et al. 1998). The *Euclid* pointing is centered on the cluster, which represents a small fraction of the total area (see Fig. 1).

---

[1] M_{200} is the mass within the virial radius, which is where the mass density of the system is 200 times the critical density of the Universe.

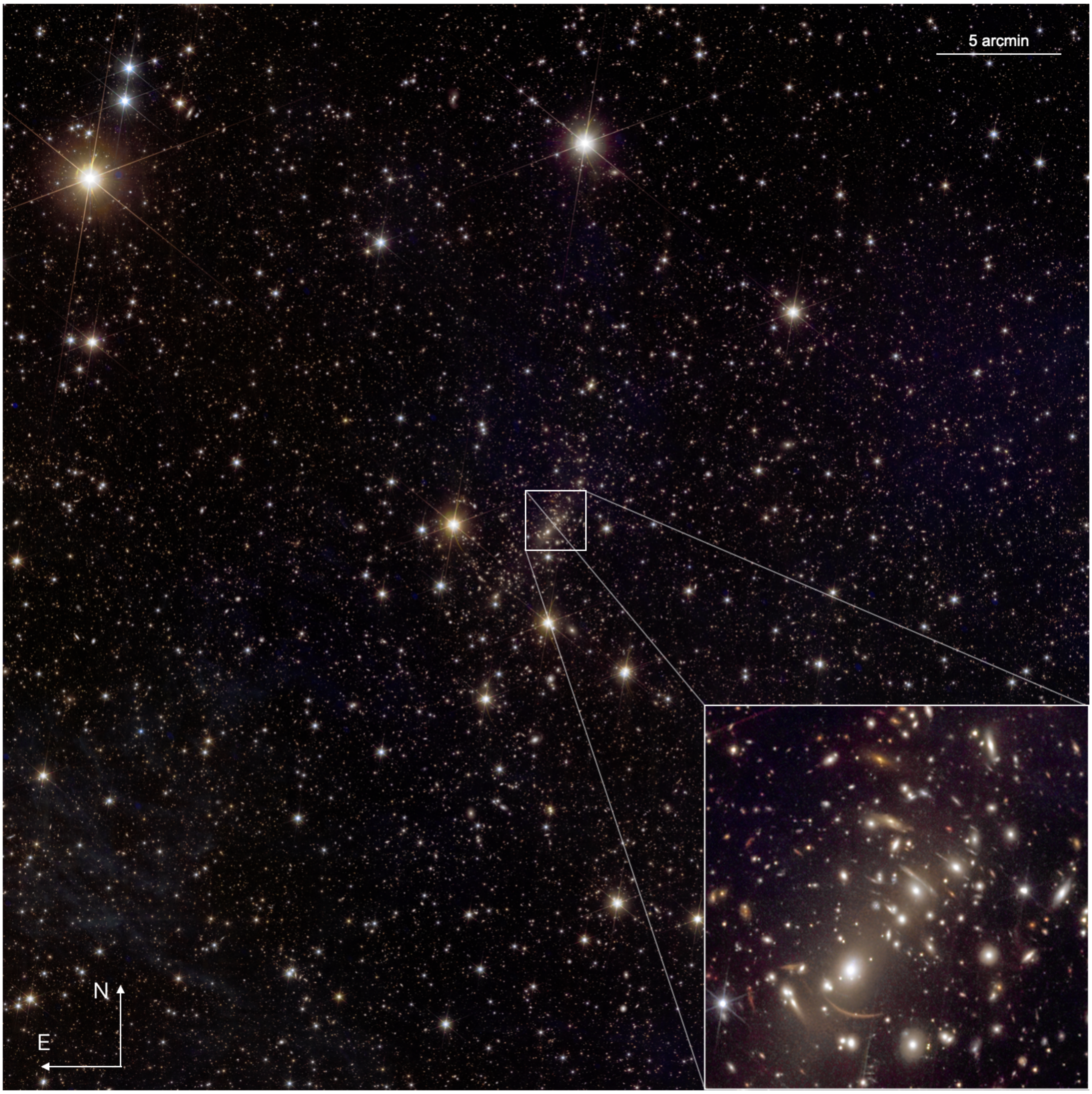

Fig. 1. *Euclid*, color-composite image of the A2390 field. The blue channel is the $I_{\rm E}$ image, the green channel is $Y_{\rm E}$, and the red channel is $H_{\rm E}$. The whole field covers about 0.5 deg^2. The inset is centered on A2390 and covers $2' \times 2'$; which is approximately the field of view of the Wide Field Camera 3 NIR channel on board HST. In the whole *Euclid*, field, approximately 250 000 sources are identified in the `CHI_MEAN` detection image based on the $Y_{\rm E}$, $J_{\rm E}$, and $H_{\rm E}$ coadded mosaic.

2.2. Abell 2764

The second ERO target was a random field on the sky that happens to cover the galaxy cluster A2764 in a corner of the field (see Fig. 2). The coordinates of the center of the field are RA=$0^{\rm h}22^{\rm m}50.1347^{\rm s}$, Dec=$-49^\circ15'59.87''$. The galaxy cluster was first identified by Abell et al. (1989). It is located at a redshift of $z = 0.07$ (Katgert et al. 1996) and is less massive ($M_{500} = 9.2 \times 10^{13}\, M_\odot$) than A2390 (Sereno & Ettori 2017). It was also far less frequently studied and characterized than A2390. Additional clusters can be identified in the field and are described in Sect. 8.

3. Observations and data reduction

3.1. Euclid observations

For each of the Abell clusters, we obtained three reference observing sequences (ROS; Euclid Collaboration: Scaramella et al. 2022), implying three times the nominal *Euclid*, wide survey exposure time. The duration of each ROS was about 70.2 min. A standard four-point dither pattern with an offset of $120'' \times 220''$ was applied for each ROS. In addition, we adopted a $3' \times 3'$ dither between the individual ROS to maximize the depth. The dithered pointings are shown in the weight maps of the NISP

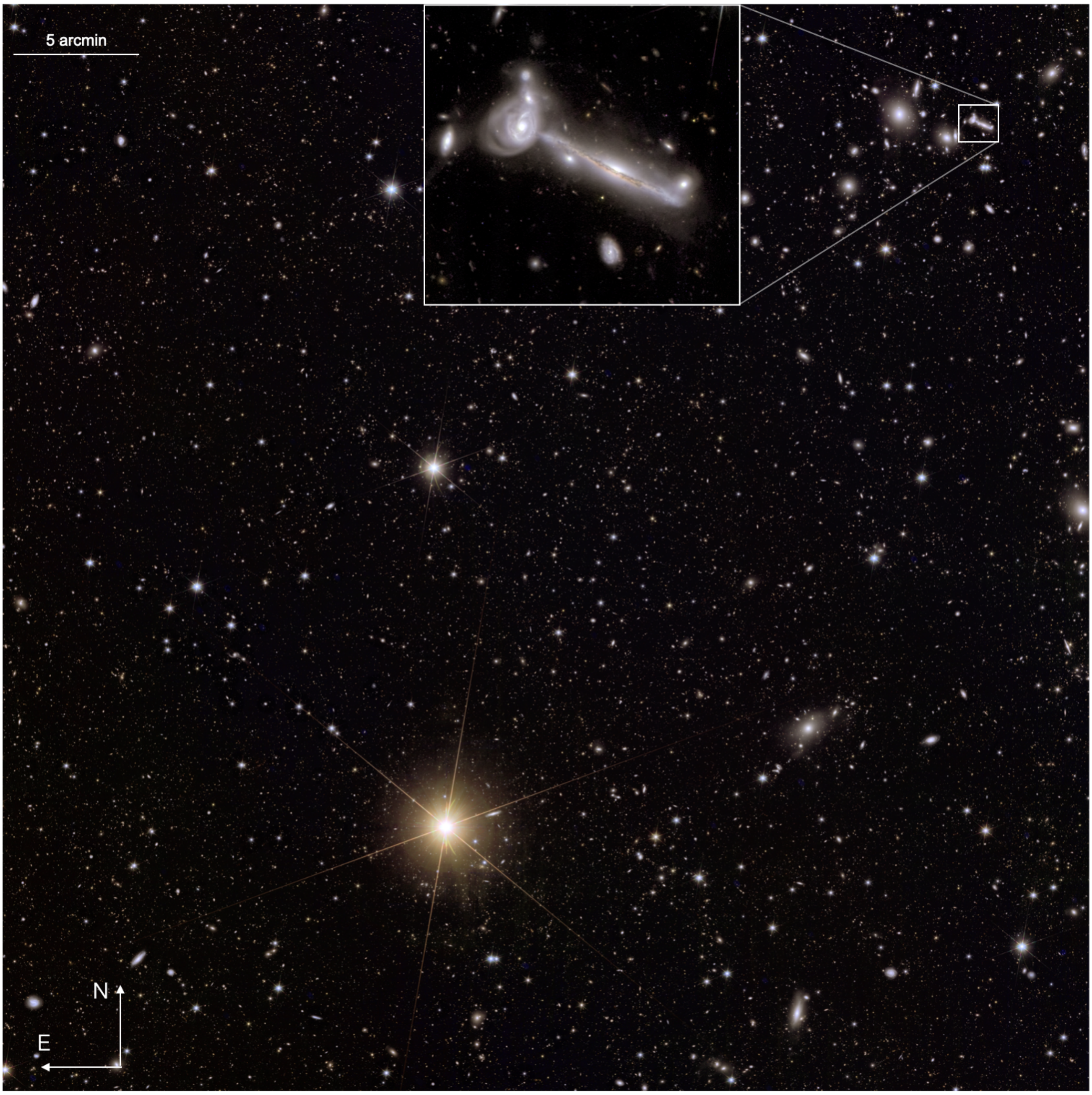

Fig. 2. Color-composite image of the A2764 field using the I_E image for the blue channel, Y_E for the green channel, and H_E for the red channel. The image field of view is about 0.5 deg^2 and contains nearly 250 000 objects based on the NISP coadded detection image. The inset shows a close-up of edge-on and face-on galaxies in the A2764 cluster.

imaging presented in Fig. 3. The large dithers fill the detector gaps and allow us to obtain a continuous coverage of the field. The field of view of each combined mosaic is about 0.75 deg^2.

The data reduction process was described in detail in Cuillandre et al. (2025). Individual frames were stacked following two different approaches. We produced compact-source stacks with the `AstrOmatic SWarp` software (Bertin et al. 2002) using the individual multiple extension fit (MEF) files and the associated weight maps. The procedure achieves an astrometric accuracy of 5.1/15.2 milliarcseconds (mas) in I_E/H_E, respectively, for A2390 and 7.9/15.8 mas for A2764. A mesh size of 64 pixels (with a smoothing factor of 3) was adopted to subtract the background in input images that feature large extended low-surface brightness (LSB) emission. The second flavor of the data reduction also used `SWarp` on the individual frames and did not perform any internal background subtraction, thereby conserving LSB features such as interstellar cirrus emission. This is particularly useful for studies of diffuse intracluster light. The sigma-clipping algorithm used to build these extended-emission stacks slightly affects the photometry of very compact sources such as stars, causing an additional 5% photometric error in this case. The images were masked to contain only overlapping

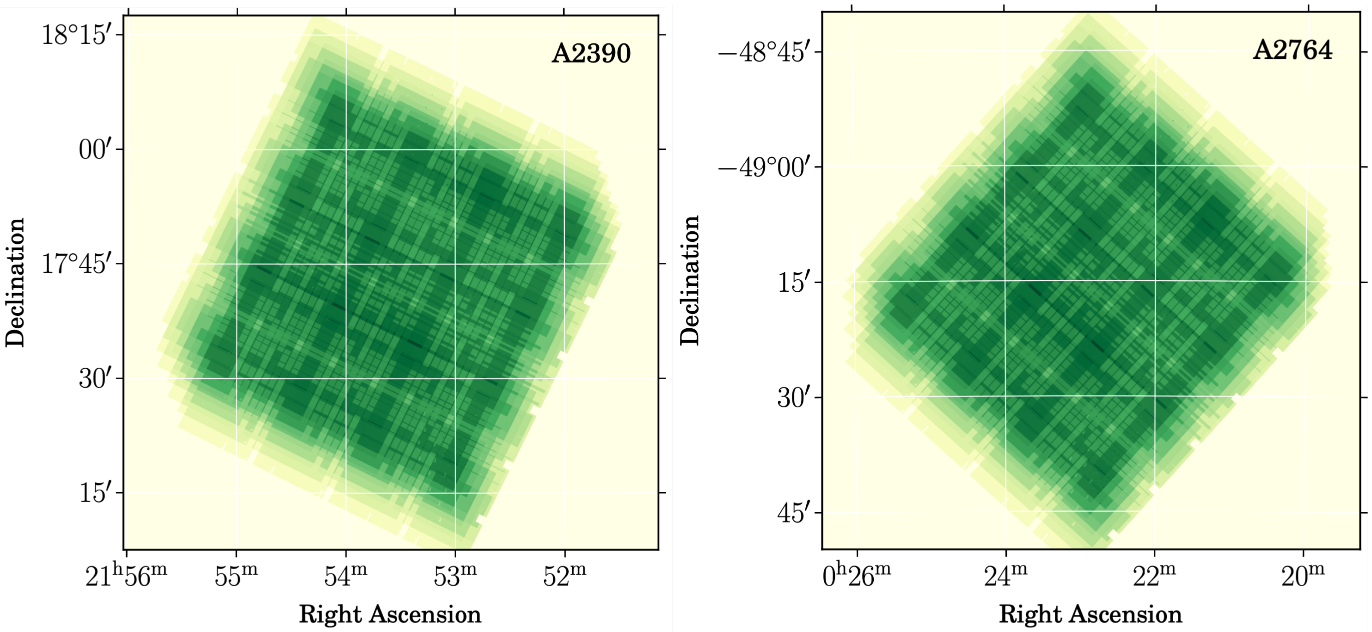

Fig. 3. Weight maps of the *Euclid*, observations of the lensing clusters A2390 (left) and A2764 (right). These examples are associated with the J_{E} observations. The maps demonstrate the large dither pattern adopted for these ERO observations and the sky coverage of each field.

regions in the dithered frames of both VIS and NISP. The final sampling of VIS and NISP images was 0.″1 pix^{-1} and 0.″3 pix^{-1}, respectively. A composite-color image of A2390 is shown in Fig. 1. The gain over the limited survey capabilities of HST in area is clear with one pointing alone. The zoom-in inset illustrates the HST/WFC3 field of view over the center of the field (the lensing cluster). The total single pointing area of 0.75 deg^2 (cropped to 0.5 deg^2 in the color image) is larger than that of the entire Cosmic Assembly Near-infrared Deep Extragalactic Legacy Survey (CANDELS) area (Koekemoer et al. 2011), which is one of the largest HST extragalactic legacy programs. We also show a composite-color image of A2764 in Fig. 2.

3.2. Ancillary observations

These two ERO fields benefit from various space-based and ground-based ancillary data. For A2390, six-band ($B, V, R_c, i, I_c,$ *and* z') imaging data (Miyazaki et al. 2002) were obtained with the Suprime-Cam instrument on the 8.2 m Subaru telescope. The data, which were reduced by the processing pipeline `SDFRED` (Yagi et al. 2002; Ouchi et al. 2004), cover a 28′ × 34′ region centered on the brightest cluster galaxy (BCG, Okabe & Smith 2016). In addition, we also considered Canada France Hawaii Telescope (CFHT) WIRCam J-band observations obtained in April, May, and September 2010. They cover the inner 24′ × 24′ region. We also considered a CFHT Megacam u-band (first-generation MP9301) image taken in August 2007 for a total integration time of 2000 s and covering the whole ERO field of view. Details of the reduction and the astrometric and photometric calibration of these ancillary data will be presented in a subsequent paper dedicated to weak lensing and photometric redshifts.

Previously, the cluster was imaged with HST using both the Wide Field Planetary Camera 2 (WFPC2) in F555W and F814W and the Advanced Camera for Surveys (ACS) in F850LP (see Ota et al. 2012). VLT/MUSE integral-field spectroscopy is also available (PID: 094.A-0115), which supports the reported strong-lensing mass modeling presented in Richard et al. (2021).

In addition, the cluster core of A2390 was observed with ALMA bands 3-5 (PID 2021.1.00766.S) and SITELLE on the CFHT (see Liu et al. 2021, and references therein), which revealed an Hα emission line in a cluster member galaxy. Furthermore, the cluster core of A2390 was mapped with the SCUBA-2 submillimeter camera by Cowie et al. (2022) to 1σ depths of 0.5 mJy at 850 µm and 2.5–3.5 mJy at 450 µm. Of the 59 submillimeter galaxies in the field, 44 have a plausible cross-identification (within 2″) in the ERO data.

Both fields were observed with the Dark Energy Camera (DECam; Flaugher et al. 2015) on the Blanco telescope at the Cerro Tololo Inter-American Observatory. A2764 lies within the footprint of the Dark Energy Survey (DES; Flaugher 2005; Dark Energy Survey Collaboration et al. 2016), with typical 10σ depths (1.″95 aperture) for the *griz* bands in DR2[2] of 24.7, 24.4, 23.8 and 23.1, respectively (Abbott et al. 2021). The typical image qualities for these DES bands are 1.″11, 0.″95, 0.″88, and 0.″83. DES data will be used to partner the southern regions of the Euclid Wide Survey during the *Euclid* first data release, and this largely blank field therefore provides an early example of these forthcoming combined data. A2390 was observed in the *grz* bands as part of the DESI Legacy Survey (DLS;[3] Dey et al. 2019). The typical depths (5σ, extended source) and image qualities of the DLS images are 23.72, 23.27, and 22.22 and 1.″29, 1.″18, and 1.″11 in the *grz* bands, respectively.

4. Photometric catalogs

4.1. Point-source aperture photometry

The combination of the NISP NIR bands (Y_{E}, J_{E}, and H_{E}) and ultradeep VIS optical imaging in I_{E}, which is about two magnitudes deeper, enables immediate searches for ultrared objects without appreciable optical flux. These objects include high-redshift galaxies and quasars ($z \gtrsim 6$) as well as dusty and/or

---

[2] `https://des.ncsa.illinois.edu/releases/dr2`

[3] `http://legacysurvey.org/`

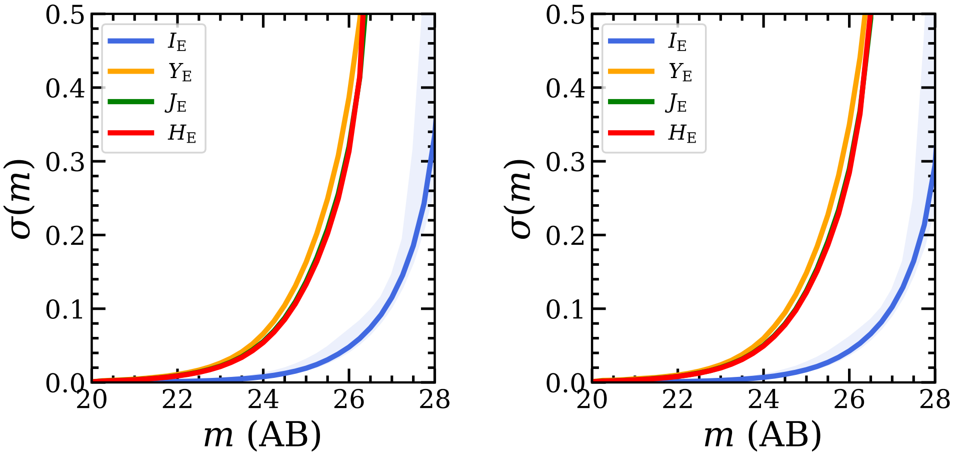

Fig. 4. Photometric errors as a function of the magnitude for all sources in the catalog for A2390 (left) and A2764 (right). Each curve represents the median error for each VIS and NISP band, and the corresponding shaded area is the 1σ dispersion. The error measurements are described in Sect. 4.1.

quiescent galaxies, cool stars, and brown dwarfs at lower redshifts. The former were a key scientific goal of this ERO program. To enable rapid searches for these objects (see Weaver et al. 2025), we first coadded the compact-source version of the $Y_{\rm E}$ +$J_{\rm E}$ +$H_{\rm E}$ mosaics to produce a `CHI_MEAN` detection image using `SWarp` (Bertin et al. 2002). In this image, we detected 501 994 objects (249 319 in A2764 and 252 675 in A2390) using the Pythonic SourceExtractor (Bertin & Arnouts 1996; Barbary 2016) assuming a threshold of $1.5\,\sigma$ within at least three contiguous pixels of the detection image, smoothed with a Gaussian kernel with a 0.″45 (1.5 pixels) FWHM[4]. The deblending was configured with 2×10^5 thresholds, requiring a contrast of 10^{-5}. No cleaning was applied as it is liable to remove real sources of interest. Photometry was extracted at the source positions by summing the pixels within several circular apertures with diameters 0.″1, 0.″2, 0.″3, 0.″6, 1.″0, 1.″2, 1.″5, and 2.″0. The uncertainties were estimated strictly from extractions from the weight map, whose distribution in effective per-pixel error matches the observed noise level in the images well. Because the NISP PSFs measured by stacking point sources in the images were similar, we corrected all apertures to the total flux, assuming point-like light distributions outside the apertures. Although we provide similarly corrected total photometry for VIS, the signal-to-noise ratio is most important for our objective, where aperture corrections are superfluous. Because of the uncertainty in recovering total fluxes, in particular, for extended objects, we therefore strongly caution against combining this photometry with other precompiled catalogs because the colors are not guaranteed to be robust. Figure 4 shows the typical magnitude uncertainty in each band as a function of magnitude for all detected sources that are included in the photometric catalog. It highlights in particular the stable photometry across a wide flux range and the significant difference in depth between the VIS and the NISP observations. The magnitude zeropoint uncertainties were estimated to be below 10% in these data. We estimated the limiting magnitude for each of the *Euclid* bands of our observations by measuring the flux in 10 000 empty apertures randomly distributed in the A2390 and A2764 images. The standard deviation of the flux distribution provides the typical depths quoted in Table 1.

Table 1. Magnitude depth of the ERO observations of the A2390 and A2764 fields.

Field	RA (deg)	Dec (deg)	$I_{\rm E}$	$Y_{\rm E}$	$J_{\rm E}$	$H_{\rm E}$
A2390	328.397	+17.709	27.01	25.18	25.22	25.12
A2764	5.713	−49.249	27.26	25.30	25.41	25.21

Notes. Limiting magnitudes are measured at $5\,\sigma$ in each *Euclid* filter assuming an aperture diameter of 0.″6 and 0.″3 for NISP and VIS, respectively.

We provide a $I_{\rm E}$,$Y_{\rm E}$,$J_{\rm E}$, and $H_{\rm E}$ photometric catalog of the two ERO fields that includes unique and field-specific IDs, coordinates, basic shape parameters, aperture and total fluxes, aperture-to-total corrections, and `SourceExtractor`-like flags. All photometric measurements were corrected for Galactic extinction using the extinction curves of Fitzpatrick & Massa (2007). A total of 73 841 unreliable sources (14.7% of the total) that probably are artifacts near mosaic edges (where only a single dither contributes to the mosaic) or near bright stars are flagged by `use_phot=0`. We refer to the accompanying `README` file for details of the source detection, photometry, and catalog contents. A case study using this catalog to identify NISP-only sources is presented in Weaver et al. (2025).

4.2. SourceXtractor++

We separately derived photometric catalogs containing the morphological parameters based on the recent reimplementation of `SExtractor` (Bertin & Arnouts 1996), called `SourceXtractor++` (hereafter `SE++`; Kümmel et al. 2022; Bertin et al. 2022). Among several other features, this code allows the user to fit PSF-convolved parametric models describing the surface brightness profile of every single source in the images. The fitting is performed simultaneously on several exposures that are grouped into a number of photometric filters or bands. The PSF and its spatial variations across the field of view were derived with the `PSFEx` tool (Bertin 2011). The characterization of the extended PSF and its spatial variation is described in detail in Cuillandre et al. (2025). In the framework of the Euclid morphology challenges (Euclid Collaboration: Merlin et al. 2023; Euclid Collaboration: Bretonnière et al. 2023),

---

[4] A discussion of thresholds and kernel sizes will be presented in Zalesky et al., in prep.

we showed that SE++ can recover accurate multiband photometry and morphological parameters, such as half-light radius, ellipticity, orientation, and Sérsic index. Mandelbaum et al. (2015) and Euclid Collaboration: Martinet et al. (2019) previously showed that recovered shapes obtained with the model-fitting engine of SExtractor meet the weak-lensing standards (with a proper weighting of the source ellipticities), which is sufficient for the scopes of cluster analysis and stage III weak-lensing surveys. A forthcoming weak-lensing study of A2390 will investigate in detail the merits of weak-lensing shape derivations with three methods: SE++, LensMC, which is currently the main cosmic shear measurement adopted for the first data release in the OU-SHE part of the *Euclid*, Ground Segment (see Congedo et al., in prep.), and KSB++ (Kaiser et al. 1995; Luppino & Kaiser 1997; Hoekstra et al. 1998).

We ran SE++ in two settings, but the source detection was always performed in the VIS I_E band. In the first run, only the VIS band was used to constrain a single Sérsic profile. This provided shapes that can readily be used for weak lensing, and the best-fit sizes provide a complementary star/galaxy discriminator. Then, a two-component bulge+disk (i.e., de Vaucouleurs + exponential) concentric model was also fit to all the ground-based, VIS, and NISP bands at once, that is, $u, B, V, Rc, i, Ic, z, I_\mathrm{E}, Y_\mathrm{E}, J_\mathrm{E}, and\ H_\mathrm{E}$. The orientation of the disk and the bulge was forced to coincide, but their axis ratios were left free. The bulge and disk half-light radii were constrained to be constant across wavelengths, but the bulge-to-total flux ratio was allowed to vary. Furthermore, in order to account for the long time span between the SuprimeCam (early 2000') and *Euclid* (November 2023) observations, we allowed for proper motions for all sources.

Both runs relied on the same PSF determination based on PSFEx. Further measurements were performed in addition to those that depend on the model fitting. In particular, aperture photometry in apertures with diameters of $1''$, $3''$, and $6''$ was computed, as well as source centroid and isophotal moments, in line with standard SExtractor measurements.

We applied a careful masking of sources in the vicinity of bright stars with an automated scaling with stellar magnitude of the size of polygons, aimed to mask out the extended diffraction spikes (Fig. 5). A model of ghosts due to reflections onto the dichroic, which splits light between the VIS and NISP instruments, was also defined. Ghosts from Gaia-DR3 stars brighter than $G_\mathrm{RP} = 12$ were automatically flagged as a disk of $8''$ radius, shifted by about $1'$ with respect to the source star. Likewise, stars (core and spikes) between Gaia magnitudes $G_\mathrm{RP} = 8.5$ and $G_\mathrm{RP} = 18.5$ were automatically masked. Since the brightness profile along diffraction spikes drops with the angular distance to the star center θ as $\theta^{-2.2}$, we scaled the size of corresponding masks as $\exp(-0.41\ G_\mathrm{RP})$. After the automated generation of the masks, further tuning was made by hand. In the case of A2390, the total relevant area before masking was 0.75 deg^2. After these regions were masked, the useful VIS area was 0.71 deg^2. The unmasked area with deep multiband SuprimeCam data was further reduced to 0.21 deg^2.

Multiband photometry at fixed positions allowed us to reach greater depth in the filters that were not the VIS I_E detection image. We reach a 0.1 magnitude uncertainty on the model magnitudes for A2390 (total bulge+disk decomposition) at 24.14, 26.19, 25.80, 26.41, 25.48, 25.64, and 24.76 for filters u, B, V, R_c, i, I_c, and z, respectively. This depth matches the *Euclid* depth well. It was achieved through exquisite observing conditions, during which the seeing reached $0\farcs905$, $0\farcs736$, $0\farcs572$, $0\farcs561$, $0\farcs516$, $0\farcs682$, and $0\farcs570$, respectively. When this is combined with VIS and NISP *Euclid* photometry, this will enable the computation of accurate photometric redshifts, as we show in the dedicated weak-lensing paper. As an illustration, we note the tight red sequence of cluster member galaxies in the left panel of Fig. 6. For details, we refer to the README file associated with the catalog release.

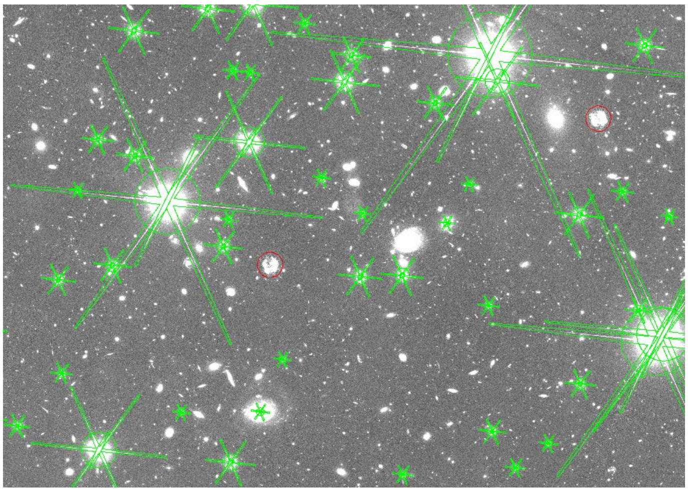

Fig. 5. *Euclid*, I_E image ($1\farcm5 \times 1\farcm0$) in the A2390 field of view, showing the masked area (inside polygons). The image shows diffraction spikes, saturation bleeds, the core region, and two reflection ghosts with a radius of $8''$ (in red).

5. High-redshift dropout sources

The relative depths of VIS and NISP imaging, which together cover the entire 0.55–2 µm spectral range, means that we can identify high-redshift ($z > 6$) dropout sources. They are well detected in NISP and remain undetected in the deeper VIS data. We present a summary of the results from the selection of high-redshift sources. A detailed analysis of these findings, along with the challenges in identifying high-redshift candidates, is provided in a dedicated paper (Weaver et al. 2025). We achieved a $5\,\sigma$ depth in the range 25.1–25.4 in the NISP bands and 27.1–27.3 in the VIS image, assuming circular apertures with a diameter $0\farcs6$ and $0\farcs3$, respectively (see Table 1). In addition, we required our sources to be detected at a $3\,\sigma$ level in the Y_E band and to be simultaneously undetected in the I_E band at a 1.5σ level. This led to a source selection that was based on a minimum Lyman break of approximately two magnitudes, which is significantly higher than most Lyman-break selection criteria used in the HST and JWST identification of $z > 6$ galaxies (e.g., Bouwens et al. 2015; Finkelstein et al. 2015; Atek et al. 2023). A stronger dropout criterion significantly reduces contamination by red low-redshift interlopers. However, ERSs can still enter our selection window, but can be differentiated from LBGs by their clearly extreme red colors compared to the relatively flat or blue UV slopes observed in LBGs above the Lyman break (see Fig. 7) and the existence of a secondary peak at low redshift in the posterior probability distribution of their photometric redshift (see below). The ERSs are an interesting population that constitutes its own science case at lower redshift. The strong Lyman break does not completely exclude some cool brown dwarf stars, especially given the limited spatial resolution of NISP, which only enables us to resolve multicomponent bright galaxies, which might be common at high redshift (Bowler et al. 2017). To minimize contamination by artifacts, we also required the sources

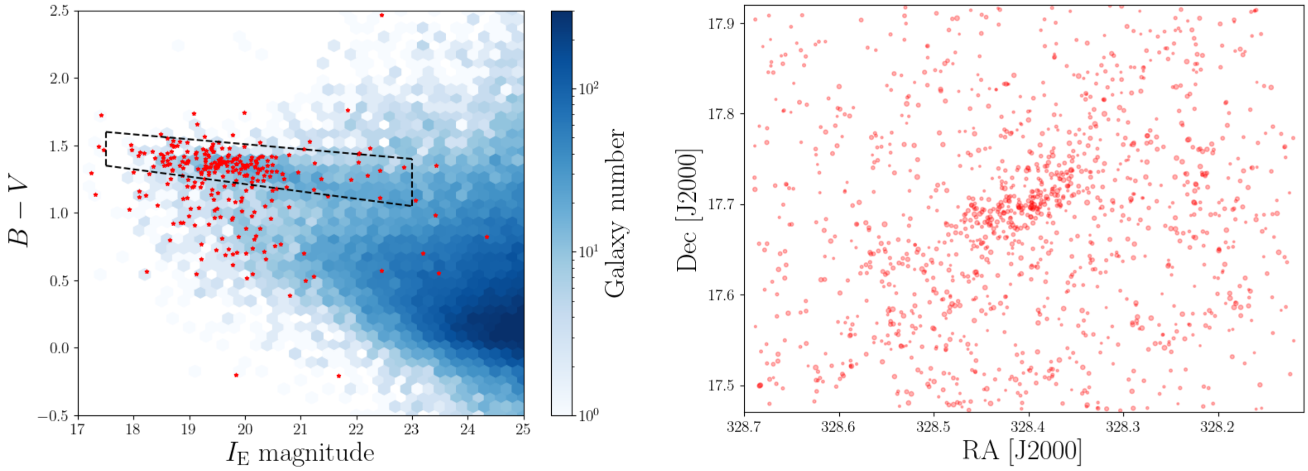

Fig. 6. Cluster members selection in A2390. Left: galaxy number density in the plane of the Subaru SuprimeCam $B - V$ color vs. *Euclid* $I_{\rm E}$-band magnitude, from bulge+disk light profile fits with `SourceXtractor++` (see text). The red stars indicate spectroscopic cluster members of A2390 determined by Sohn et al. (2020) and MUSE observations of the core of A2390. The dashed region indicates the cluster red sequence based on the spectroscopic members and extrapolated to fainter magnitudes. Right: sky location of galaxies enclosed by the red-sequence selection in the left panel over the joint 0.21 deg^2 area covered by *Euclid* and Subaru SuprimeCam. The size of each point scales inversely with $I_{\rm E}$ magnitude to indicate the distribution of stellar mass in red galaxies at the cluster redshift.

to be compact by imposing a flux ratio of two apertures of $J_{\rm E}$ $(1\farcs5)/J_{\rm E}$ $(0\farcs6) < 1.3$. We verified that the criterion does not exclude real sources from the selection. Furthermore, in order to mitigate contamination by persistence at NIR wavelengths from previous exposures, we performed a time-series analysis on the individual frames. We removed all sources that showed a typical declining light curve (for more details, see Weaver et al. 2025).

This color selection was complemented with photometric redshift estimates using the spectral energy distribution (SED) fitting tool `eazy-py` (Brammer et al. 2008, 2022). We assumed a redshift range of $0.01 < z < 15$ and a flat luminosity prior using the `agn_blue_sfhz` set of galaxy templates. All the sources have a posterior distribution function (PDF) that is consistent with the $z > 6$ solution, without a significant secondary solution at low redshift. The full procedure and the dropout sample are described in detail in Weaver et al. (2025). Combining the two ERO fields, we identified a total of 30 LBGs and 139 ERSs from a total of about 500 000 sources. The absolute magnitudes of the LBGs ranges between $M_{\rm UV} = -21.9$ and $M_{\rm UV} = -23.6$. In Fig. 7, we show an example for each of these categories. The top row shows the photometry in each of the NISP and VIS filters and a composite-color image of the $Y_{\rm E}$, $J_{\rm E}$, and $H_{\rm E}$ images. We also show the best-fit solutions of the photometric data derived with `eazy-py` and the associated probability distribution. The LBG candidate has a clear high-redshift solution centered at $z \sim 7.7$, and the ERS has a significant low-redshift solution around $z \sim 1.7$.

These early results, based on a small portion of the sky relative to the full survey, highlight the crucial role that *Euclid* will play in identifying the brightest galaxies during the epoch of reionization. Given the uncertainties on the exact shape of the bright-end of the UV luminosity function at $z \sim 8$–10 (Bowler et al. 2020) on the one hand and the apparent excess of UV-bright galaxies at $z > 10$ (Harikane et al. 2023; Chemerynska et al. 2024; Adams et al. 2023; Donnan et al. 2024) on the other hand, *Euclid* imaging and subsequent spectroscopic follow-up will be instrumental in constraining the exact abundance of bright high-redshift galaxies and the exact shape of the bright end of the UV luminosity function at z =6–9. The cross-correlation with Lyα emitters will allow the identification of giant ionized bubbles with sizes of about 10 Mpc and map the ionization state of the IGM. In addition to bright LBGs, the *Euclid* data will also allow us to identify bright quasars in the deep and wide surveys. The ability of the current data to distinguish between high-redshift quasars and galaxies remains limited in the absence of follow-up spectroscopy. *Euclid* grism spectroscopy will be limited to sources brighter than 22 mag. These limitations also apply to potential contaminating sources at low redshifts, such as cool brown dwarf stars (Weaver et al. 2025). Again, the relative depth of VIS imaging compared to NISP, which leads to very strong breaks between these two wavelengths, reduces the contamination rate of Galactic dwarfs, but will remain an important source of contamination (Euclid Collaboration: Barnett et al. 2019). Fortunately, the brightness of these sources makes them ideal candidates for follow-up spectroscopy from the ground in order to confirm their redshifts. Determining the number, density, and luminosity of these sources will motivate follow-up campaigns with JWST, for example, to constrain the nature of the brightest sources in the early Universe, including galaxies and quasars.

6. Weak-lensing analysis

Weak gravitational lensing (WL) is one of the primary cosmological probes of *Euclid*. By measuring the shapes of background galaxies, WL analyses allow the reconstruction of the projected foreground mass distribution (e.g., Bartelmann & Schneider 2001), which is dominated by invisible dark matter. The WL signature of one of the targets of this ERO program, A2390, has previously been studied using ground-based WL data (e.g., von der Linden et al. 2014; Applegate et al. 2014; Okabe & Smith 2016). However, given their outstanding depth and resolution, the new *Euclid*, observations of the cluster provide an excellent opportunity to show the WL capabilities of *Euclid*. To do this, we measured WL galaxy shapes in the A2390 VIS observations using different shape-measurement algorithms including `LensMC` (which is designated as the primary shape measurement of the *Euclid* Data Release 1), `SE++` (see Sect. 4.2), and `KSB+` (Kaiser et al. 1995; Luppino & Kaiser 1997; Hoekstra et al.

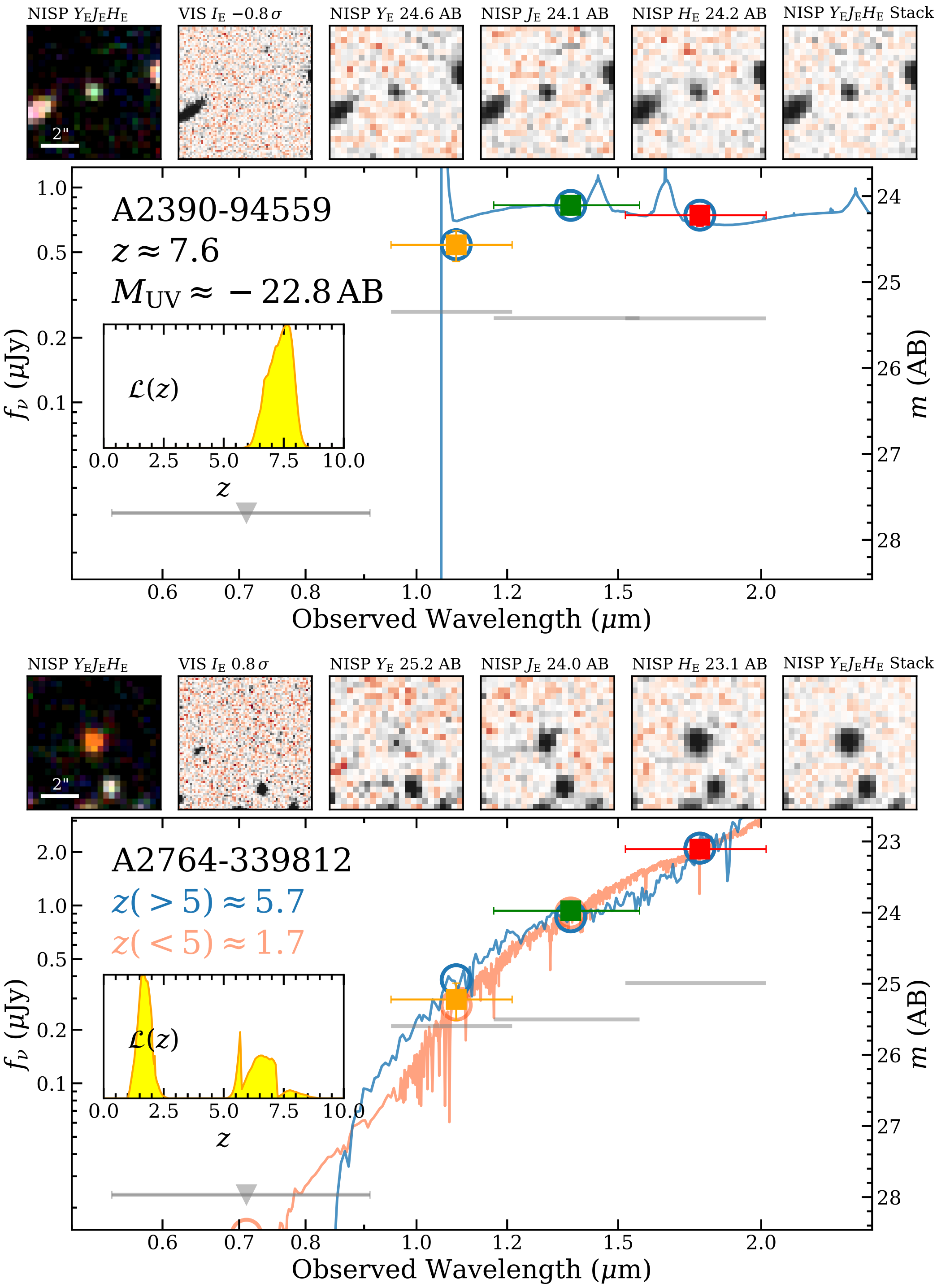

Fig. 7. Identification of VIS-dropout candidates in the A2390 and A2764 fields. The top panel shows an example of an LBG candidate at a redshift of $z > 6$, and the bottom panel shows an ERS, most likely located at a lower redshift. For each of these sources, the top row shows the cutout images of the source in the VIS and NISP filters, together with an NISP stack and a color-composite image based on the Y_E, J_E, and H_E filters. The size of these images is about 7″ × 7″. The bottom panel illustrates the best-fit model (blue and orange curves) to the *Euclid* photometry (colored circles with associated 1 σ uncertainties). The gray horizontal bars denote the 3 σ depth of each band, while the down-pointing triangle marks the upper limit of the I_E band. The left inset presents the posterior distribution function for the photometric redshift (see Weaver et al. 2025, for details).

1998). The details of this analysis will be presented in a separate paper. Here, we briefly highlight the first results from the `KSB+` analysis, which employs the Erben et al. (2001) implementation of the `KSB+` algorithm, including the shear bias calibration from Hernández-Martín et al. (2020), as used, for example, for the analysis of HST WL observations of distant galaxy clusters from the South Pole Telescope in Schrabback et al. (2018, 2021), and Zohren et al. (2022). After applying the `KSB+` shape measurement selections, removing masked objects in the vicinity of bright stars (see Sect. 4.2) and very extended galaxies, and requiring a flux signal-to-noise ratio S/N > 10 (defined as the `FLUX_AUTO`/`FLUXERR_AUTO` ratio from `SExtractor`), as well

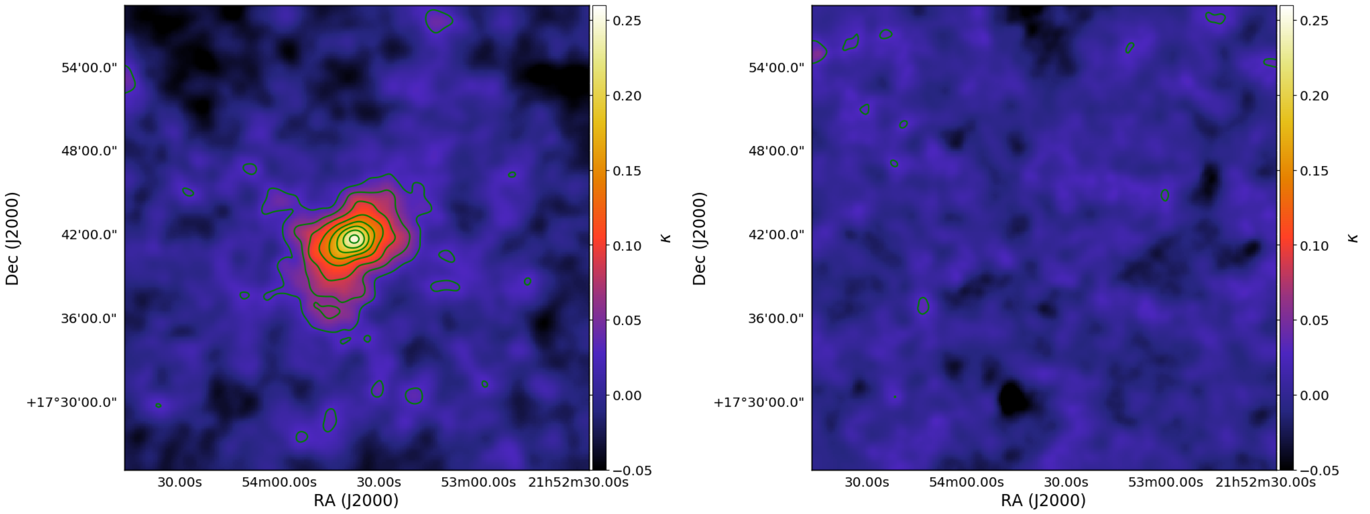

Fig. 8. WL convergence κ reconstruction of the A2390 field. The left panel shows the reconstructed E-mode signal, with the cluster detected in the central region with high significance. The right panel shows the B mode, which does not include a cosmological signal to first order, but provides an illustration of the noise level of the reconstruction. The green contours start at $\kappa = 0.03$ and are in steps of $\Delta\kappa = 0.03$. Both reconstructions assume a zero mean convergence when averaged over the full reconstructed sky area.

as a magnitude in the range $22 < I_{\mathrm{E}} < 26.5$, the resulting catalog provides a WL density of 56.5 sources per arcmin^2 when averaged within the central $33\farcm3 \times 33\farcm3$ region around the cluster center. As an initial result of this analysis, we present a reconstruction of the convergence field κ in Fig. 8. The convergence maps the foreground mass distribution, but is scaled according to the geometric lensing efficiency (e.g., Bartelmann & Schneider 2001). In particular, we applied a Wiener-filtered reconstruction following the procedures described in McInnes et al. (2009), Simon et al. (2009), and Schrabback et al. (2018). Here, the signature of the cluster is detected with high significance in the curl-free E-mode reconstruction (left panel of Fig. 8). In the right panel of Fig. 8, we additionally show a B-mode reconstruction derived from the curl component of the WL shear field. To first order, gravitational lensing only creates curl-free E modes. Accordingly, the B-mode reconstruction provides an assessment for the level of noise (and potential residual systematics) in the reconstruction.

7. Weak- and strong-lensing analysis

Euclid WL data can be combined with existing strong-lensing (SL) constraints (or new multiple-image systems identified by *Euclid*), enabling a joint SL+WL analysis. SL constraints are useful to constrain the inner cluster regions (typically, the central 300 kpc), but do not constrain the outer cluster regions. This limits our ability to estimate their virial masses. The *Euclid* WL measurements can extend the analysis of the lensing signal to beyond the virial radius. When several multiply imaged galaxies exist at different redshifts, the combination of the two datasets breaks the mass-sheet degeneracy (e.g., Schneider & Er 2008). Among the ERO targets, A2390 offers a unique opportunity to test the capacity of *Euclid* at measuring the virial mass of a massive cluster. This cluster contains 11 multiply imaged galaxies with confirmed spectroscopic redshifts (Richard et al. 2021). These galaxies produce 23 multiple images that result in 46 SL positional constraints. We combined these constraints with WL measurements from *Euclid*. We rebinned the WL data in $\sim 1 \times 1$ arcmin^2 bins near the center to $\sim 3 \times 3$ arcmin^2 bins near the edges.

The analysis was performed with the free-form code `WSLAP+` (Diego et al. 2007; Sendra et al. 2014). This algorithm assumes that the mass distribution can be decomposed as a superposition of 2D Gaussian functions. The amplitude of each Gaussian was optimized by minimizing the difference between the observed and predicted lensing variables (mean shear in the adopted bins for the WL portion of the dataset, and positions of multiply imaged galaxies for the SL portion of the dataset). The unknown position of the multiply imaged galaxies in the source plane was also optimized together with the distribution of mass. In the inner portion of the region constrained by the SL measurement, the light distribution of the most prominent member galaxies (approximately 70 for this cluster) was assumed to trace the mass on small scales with a given mass-to-light ratio, which was also derived as part of the optimization. The resulting convergence profile is shown in Fig. 9, where we show the solution obtained when only SL data are used and when both SL and WL data are used. The profile in the inner region ($R \lesssim 0.44$ Mpc) contains the contribution from the member galaxies. Even though member galaxies contribute only little to the profile of the convergence (except in the central peak), these galaxies are relevant for an accurate prediction of the positions of the multiply imaged lensed galaxies, and they also act as a regularization mechanism for the solution to converge (see Diego et al. 2007; Sendra et al. 2014). The SL+WL profile differs significantly from the SL profile at radii beyond the region constrained by SL because the SL-only solution is not constrained in this regime, where `WSLAP+` solutions are known to be biased low (this is a memory effect of the initial guess as described in Diego et al. 2007). In contrast, the SL+WL combination recovers a solution consistent with the expected Navarro-Frenk-White (NFW) profile (Navarro et al. 1996) of massive clusters at large radii.

8. *Euclid* preview of high-redshift galaxy clusters detected in the field of A2764

In order to illustrate the unique capabilities of *Euclid* to detect high-redshift ($z > 0.6$) galaxy clusters, we searched for concentrations of galaxies in the VIS and NISP images in the direction of already known high-redshift clusters. To do this, we focused

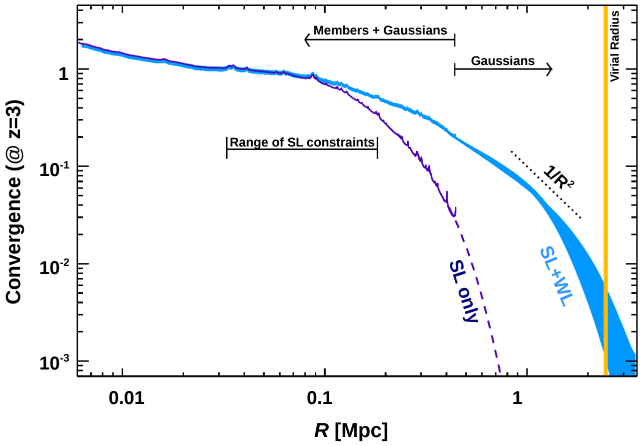

Fig. 9. Mass profile of A2390 from an SL-only analysis and a joint SL+WL analysis. The two regions that include members+Gaussians ($R \lesssim 0.44$ Mpc) in the lens model or only Gaussian functions are indicated. We also show the range of distances covered by the SL constraints (from the brightest cluster galaxy). For the SL+WL combination, we show a range of models that are consistent with the data (~1 standard deviation). The addition of WL data from *Euclid* is key to properly constrain the mass of the cluster out to the virial radius (corresponding to R_{200} or to the radius at which the density reaches 200 times the mean density of the Universe) with a vertical orange bar, where the width is the uncertainty in the virial radius.

on the increasingly large numbers of clusters that are blindly detected with surveys in the millimeter spectral range via the Sunyaev–Zeldovich effect (SZ; Sunyaev & Zeldovich 1972b,a, 1980; Planck Collaboration XIII 2016; Planck Collaboration Int. XLVII 2016; Bleem et al. 2024) and in the X-ray range (e.g., Bulbul et al. 2024). More specifically, we used ground-based telescopes such as the Atacama Cosmology Telescope (ACT; e.g., Hilton et al. 2021) and the South Pole Telescope (SPT; e.g., Bleem et al. 2015), which allowed us to detect clusters out to $z \sim 1.9$. We also made use of the eROSITA-DE DR1 point and extended sources (Merloni et al. 2024). As shown in Bulbul et al. (2024), the first release of eROSITA data is already able to identify groups and clusters at high redshift, out to $z \sim 1.3$.

The ERO field of A2764 is located in both the ACT and SPT footprints. We searched for the presence of clusters from these two surveys in the ERO observation. We found that the A2764 ERO field contains a few background galaxy clusters that were previously detected in SZ with masses $M_{500} \sim 2 \times 10^{14}\,M_{\odot}$, located in the redshift range $z \sim 0.6$–0.7, which is higher than the target cluster. Three of them are ACT clusters (Hilton et al. 2021, DR5): (1) ACT-CLJ0022.5−4843 is an ACT-only cluster at $z_{\rm phot} = 0.855 \pm 0.015$ with an estimated mass of $M_{500} = 1.71^{+0.37}_{-0.30} \times 10^{14}\,M_{\odot}$; (2) ACT-CLJ0021.5−4902 at $z_{\rm spec} = 0.688$ and $M_{500} = 2.35^{+0.45}_{-0.38} \times 10^{14}\,M_{\odot}$ is also identified as SPT cluster SPT-CLJ0021.5−4902 (see Bleem et al. 2015; Everett et al. 2020), and it is associated with an eROSITA point source (see below); and (3) ACT-CLJ0023.7−4923 has a photometric redshift $z_{\rm phot} = 0.709 \pm 0.021$ and a mass $M_{500} = 1.88^{+0.41}_{-0.33} \times 10^{14}\,M_{\odot}$. These three clusters are clearly identified in the VIS and NISP images as concentrations of galaxies. Moreover, we note that both ACT-CLJ0023.7−4923 and ACT-CLJ0021.5−4902 show strong gravitational lensing features in both the VIS and NISP images (see Figs. 10 and 11). To our knowledge, only the strong lensing in ACT-CLJ0023.7−4923 was previously known (Diehl et al. 2017), and thus, the strong lensing observed in ACT-CLJ0021.5−4902 is a first detection for this cluster. Finally, a faint SPT source, SPT-SJ002330−4947.3, detected at 150 GHz (Everett et al. 2020), is located near the noisy edge of the A2764 *Euclid* ERO field. The quality of the images does not allow us to identify the possible visible or NIR counterparts.

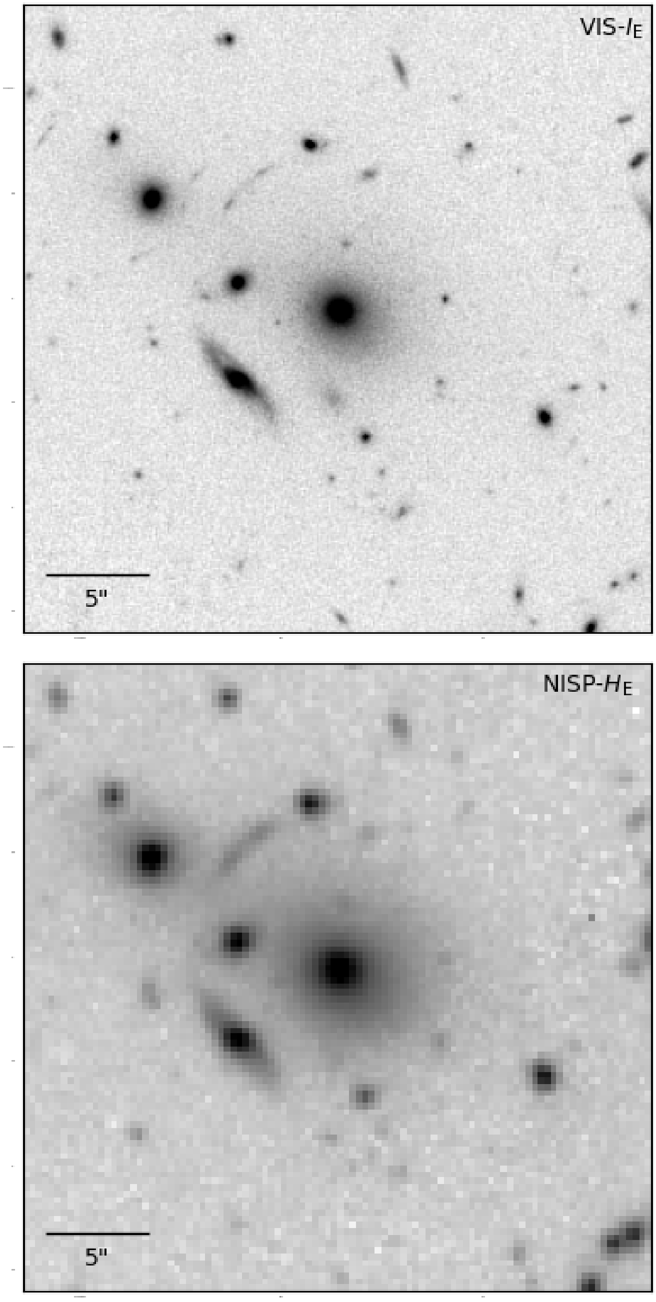

Fig. 10. 30″×30″ cutout centered on the galaxy cluster ACT-CLJ0021.5−4902 at $z_{\rm spec} = 0.688$, associated with the eROSITA DR1 source 1eRASSJ002132.6−490216, as seen in VIS $I_{\rm E}$ (top panel) and NISP $H_{\rm E}$ (bottom panel). A strong-lensing arc that was previously unknown is clearly identified.

More than 40 point and extended sources from the eROSITA DR1 catalog (Merloni et al. 2024) are found in the A2764 ERO field. The cluster A2764 itself is one of the eROSITA DR1 sources in the field. It appears as the two extended sources 1eRASSJ002035.1−491245 and

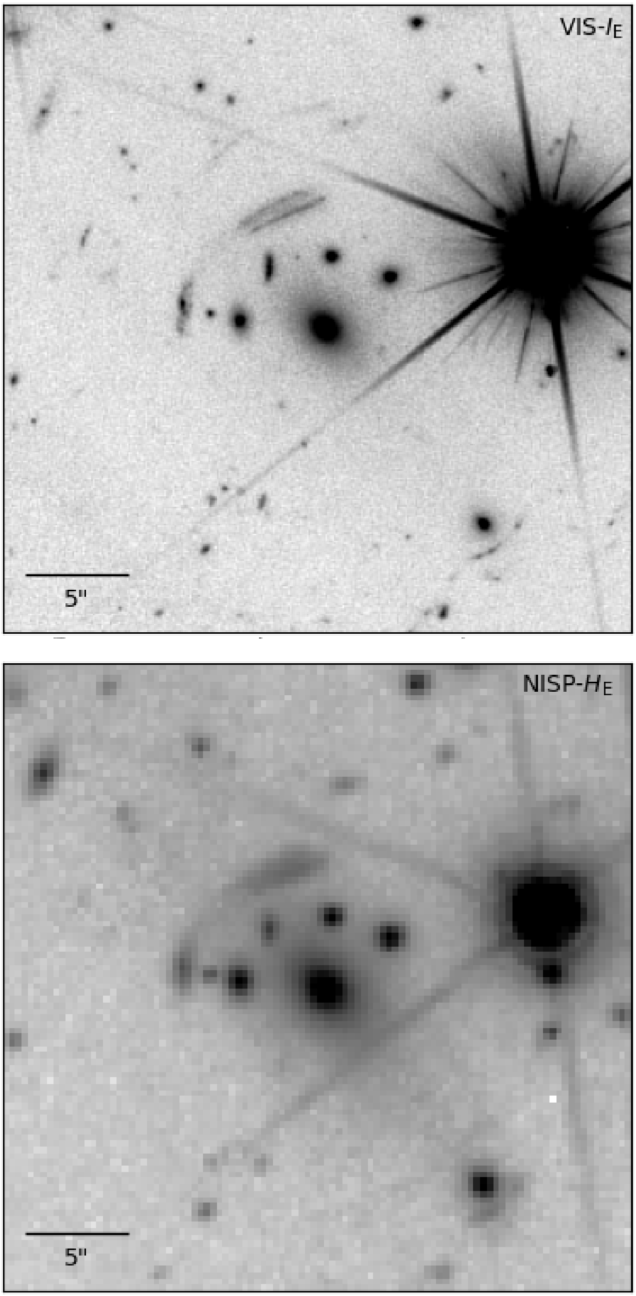

Fig. 11. 30″×30″ cutout centered on the galaxy cluster ACT-CLJ0023.7−4923 with z_phot = 0.709 ± 0.021, associated with the eROSITA DR1 source 1eRASSJ002345.0−492354, as seen in VIS I_E (top panel) and NISP H_E (bottom panel). Multiple lensing features, which are already known, are visible in the image. The star to the right of the image is *Gaia* 4973928409193111936 of G_RP = 14 mag.

1eRASSJ002032.1−491432. The two ACT galaxy clusters (Hilton et al. 2021) are matched with eROSITA DR1 point sources: ACT-CLJ0021.5−4902 at z_spec = 0.688 is associated with 1eRASSJ002132.6−490216 (IDCluster=758, EXT=0), and ACT-CLJ0023.7−4923 at z_phot = 0.709 ± 0.021 is associated with 1eRASSJ002345.0−492354 (IDCluster=273 EXT=0). Only one source labeled as extended in the eROSITA DR1 catalog is found in the A2764 ERO field and would qualify as a galaxy cluster: 1eRASSJ002223.6−492746 (with IDCluster=183, EXT=19.3 and EXT_LIKE=3.07). The VIS and NISP images show concentrations of galaxies at the associated location, and the distribution of photometric redshifts indicates a peak at $z_\mathrm{phot} \sim 0.8$. We also checked for counterparts in the Massive and Distant Clusters of WISE Survey (MaDCoWs) catalogs (Gonzalez et al. 2019) and found no match in the ERO A2764 field.

Another remarkable eROSITA DR1 point source is 1eRASSJ002212.5−492811 (IDCluster=47 EXT=0). It is less than 2′ away from the aforementioned source 1eRASSJ002223.6−492746, and about 40 VIS and NISP galaxies are located in its vicinity, half a dozen with a photometric redshift peaking at $z_\mathrm{phot} \sim 0.8$, and about 30 at $z_\mathrm{phot} \sim 1.4$. Although the association of *Euclid* galaxies and this eROSITA source is not yet confirmed, it illustrates the power of the *Euclid* survey in combination with other wavelength datasets to efficiently provide robust galaxy cluster candidates.

This simple search for optical and near-IR counterparts to already known SZ clusters at $z > 0.6$ with $M_{500} > 10^{14}\,M_\odot$ in this ERO program data demonstrates that *Euclid* VIS and NISP instruments are particularly efficient at detecting clusters at $z > 0.6$. Matching with eROSITA extended and point sources also opens the way for the detection of new clusters at potentially even higher redshifts. Further work is needed to confirm associations between optical and NIR *Euclid* galaxies with millimeter or X-ray-detected clusters. Dedicated cluster-finding algorithms also need to be run to find galaxy clusters and protoclusters in the *Euclid* data. Nevertheless, this first analysis demonstrates that *Euclid* data will be a treasure trove for cluster studies.

9. Intracluster light

Intracluster light (ICL) is diffuse light seen in galaxy groups and clusters. It comes from stars that are bound to the gravitational potential well of the cluster and not from any particular galaxy (see Contini 2021; Montes 2022, for reviews). It is a prominent feature observed in clusters (e.g., Feldmeier et al. 2004; Kluge et al. 2020; Golden-Marx et al. 2023), and the origin and assembly history of the ICL serves as a tool for characterizing the assembly history of the brightest central galaxy and the satellite galaxy population (e.g., Murante et al. 2007). In addition, the ICL can be used as a luminous tracer of the dark matter distribution within the cluster (Montes & Trujillo 2019; Alonso Asensio et al. 2020; Deason et al. 2021; Gonzalez et al. 2021; Yoo et al. 2022; Contreras-Santos et al. 2024).

Although the ICL appears to be a powerful tool for studying galaxy clusters and cosmology, our understanding of this component has been hampered by observational limitations. For example, ground-based observations have been challenging due to the extreme faintness of this emission. HST has provided ultra-deep images of galaxy clusters, but it has a clear limitation: its small field of view. The high-resolution space-based images of *Euclid* can characterize the ICL beyond the typical HST limit of 100–200 kpc and will help us to improve our understanding of the formation of this diffuse light and the assembly of clusters. In this sense, *Euclid* can finally provide the wide field of view needed to probe the outer cluster regions. Using observations from this ERO program, we will probe the ICL of A2390, A2764, and the other high-redshift clusters detected in the field of A2764 out to distances of several hundred kiloparsec.

Figure 12 shows the extent and distribution of the ICL surrounding A2390 in the H_E band. We used the outer PSF model of Cuillandre et al. (2025) to subtract the PSF contribution of several bright stars in the field. To highlight the

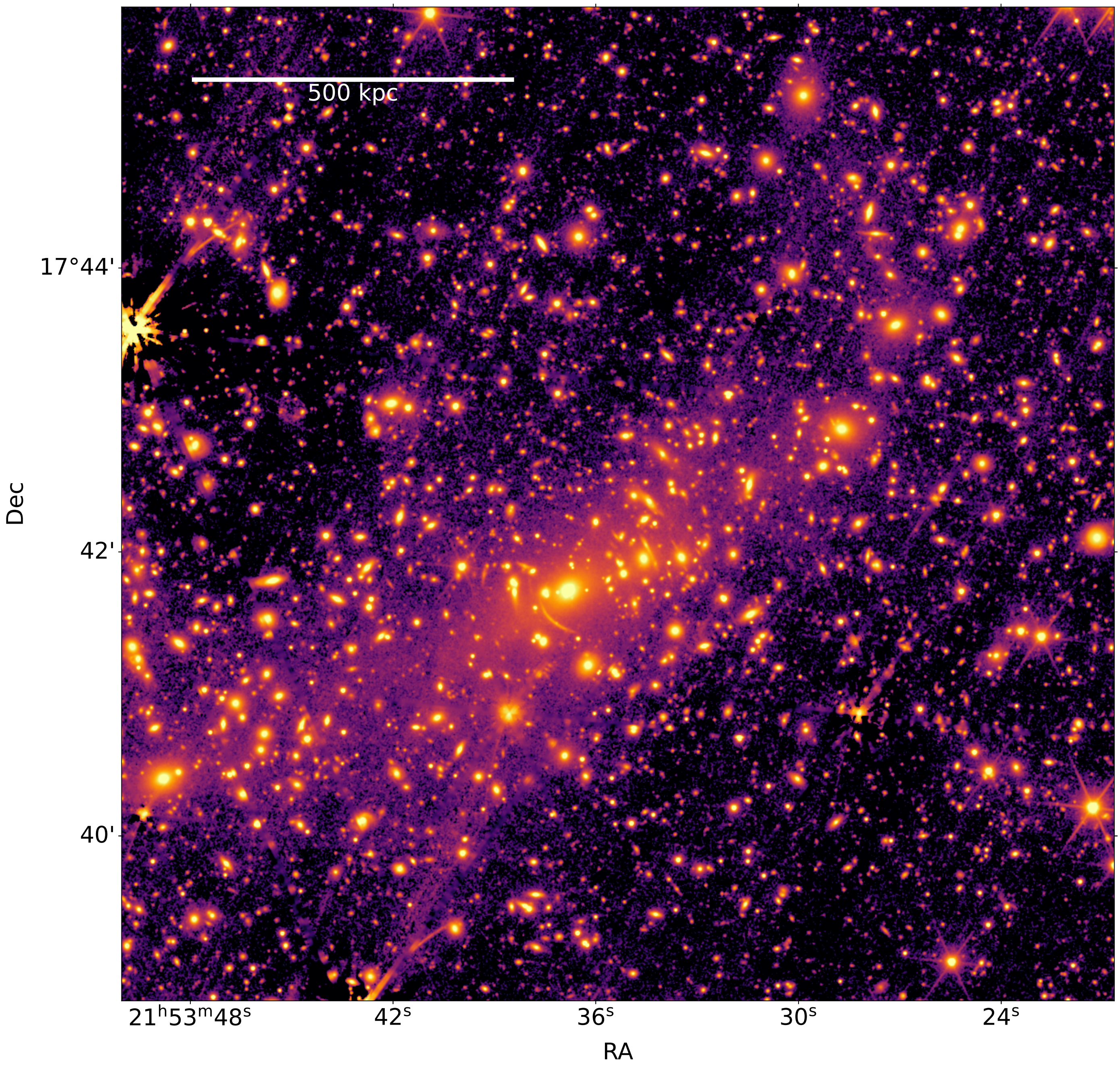

Fig. 12. H_{E}-band image showing the extent of ICL in A2390. The stars in the field were subtracted using the PSF model of Cuillandre et al. (2025), and the diffraction spikes were masked by hand. The lognormal color scale was chosen to highlight the diffuse ICL in this cluster.

low surface-brightness ICL, we masked the remaining diffraction spikes by hand and interpolated over the masked pixels using a Gaussian kernel with $\sigma = 0\farcs6$. The ICL stretches over approximately 1 Mpc from the southwest to the northwest, following the distribution of the brightest members of the cluster. The 1σ image depth is $\mu(H_{\mathrm{E}}) = 28.88\,\mathrm{mag\,arcsec^{-2}}$ measured over a $10'' \times 10''$ area (see Cuillandre et al. (2025) for details). At this depth, the main sources that limit the reliability of the ICL measurement are Galactic cirri and noise from the subtraction of the NIR persistence. The ERO data for the Perseus cluster reached a similar depth as these ERO data on A2390 and A2764 (Cuillandre et al. 2025). The ICL of the Perseus cluster was reliably measured out to a semimajor axis distance of 600 kpc, reaching a $1\,\sigma$ depth of $\mu(I_{\mathrm{E}}) = 29.4\,\mathrm{mag\,arcsec^{-2}}$, $\mu(Y_{\mathrm{E}}) = 28.4\,\mathrm{mag\,arcsec^{-2}}$, and $\mu(J_{\mathrm{E}}) = \mu(H_{\mathrm{E}}) = 28.7\,\mathrm{mag\,arcsec^{-2}}$ (Kluge et al. 2025) in similar cirrus conditions and significantly more persistence (due to larger galaxies in the field of view). Hence, we expect to reach similar depths in these images.

10. Summary

The ERO program presents an opportunity to highlight the capabilities and performance of the *Euclid* spacecraft. It offers a glimpse of the nominal survey observations. In this paper, we used data acquired from the ERO11 program that focused on two lensing clusters, A2390 and A2764. The nature and depth of these data enable an exploration of various scientific cases related to galaxy formation and evolution, weak- and strong-lensing phenomena, as well as the physics of galaxy clusters. We produced a photometric catalog in I_E, Y_E, J_E, and H_E bands for a total of 501 994 sources using different aperture sizes. We also performed multiband photometry based on VIS detections, which include supporting ground-based observations. These catalogs are made publicly available along with this paper.

The combination of NISP and VIS imaging is well suited for identifying dropout sources that are visible only in the NISP images and remain undetected in the optical I_E filter. This is particularly relevant for detecting the Lyman break of high-redshift sources at $z > 6$ because the survey design naturally produces roughly three magnitude breaks. Combining photometric criteria with SED fitting with `Eazy`, we identified a total of 30 LBG candidates. The compactness of these sources, which remain unresolved in the NISP images, presents a challenge in discriminating between galaxies and quasars. Furthermore, despite exhibiting an apparently pronounced Lyman break, certain rare brown dwarfs can display colors that resemble those of our targeted sources. Nevertheless, considering that *Euclid* possesses the unique capability to efficiently identify these bright and rare sources on the sky at $z > 6$, it becomes clear that this will facilitate extensive spectroscopic follow-up campaigns from both ground- and space-based observatories, enabling the confirmation of their redshifts and the study of their physical characteristics.

These cluster fields also offer the possibility to perform a joint SL+WL analysis to model the mass distribution of these structures. We combined an already existing SL model of A2390 with our own WL analysis to extend the constraints to larger radii and to estimate the virial mass of the cluster better. Using the `WSLAP+` code, we showed that WL improves the mass profile reconstruction of the cluster compared to SL alone.

We also illustrated the potential of *Euclid* to detect high-redshift galaxy clusters by using these ERO data to search for optical and NIR counterparts of known clusters. In particular, we identified three clusters in the A2764 field that were previously detected by their X-ray emission (eROSITA) or by the SZ effect (ACT and SPT). Two of the three clusters, which are located at $z = 0.6$–0.9, show clear gravitational lensing features. This early work already demonstrated the ability of multiwavelength efforts to discover high-redshift clusters and to calibrate automatic identification algorithms in the near future.

Finally, cluster fields are ideal laboratories for studying the ICL, which helps us to constrain the assembly history of cluster galaxies and to indirectly map the dark matter distribution. We illustrated the large extent of the ICL in A2390 visible in the *Euclid* images, which go far beyond the limited field of view of HST.

Overall, this paper underscores the large array of scientific studies that will be carried out in blank (but also lensed) fields with *Euclid*. The depth, angular resolution, and wide field of view are clearly a unique combination that will push many frontiers in the landscape of the *Euclid* legacy science.

Acknowledgements. HA is supported by the French Centre National d'Etudes Spatial (CNES). The Cosmic Dawn Center (DAWN) is funded by the Danish National Research Foundation (DNRF140). This work has made use of the `CANDIDE` Cluster at the *Institut d'Astrophysique de Paris* (IAP), made possible by grants from the PNCG and the region of Île de France through the program DIM-ACAV+, and the Cosmic Dawn Center and maintained by S. Rouberol. HM is supported by JSPS KAKENHI Grant Number JP23H00108, and JSPS Core-to-Core Program Grant Numbers JPJSCCA20200002 and JPJSCCA20210003. MJ is supported by the United Kingdom Research and Innovation (UKRI) Future Leaders Fellowship 'Using Cosmic Beasts to uncover the Nature of Dark Matter' (grants number MR/S017216/1 & MR/X006069/1).TS acknowledges support provided by the Austrian Research Promotion Agency (FFG) and the Federal Ministry of the Republic of Austria for Climate Action, Environment, Energy, Mobility, Innovation and Technology (BMK) via the Austrian Space Applications Programme with grant numbers 899537 and 900565, as well as the German Research Foundation (DFG) under grant 415537506, and the German Federal Ministry for Economic Affairs and Climate Action (BMWK) provided by DLR under projects no. 50QE2002 and 50QE2302. This work has made use of the Early Release Observations (ERO) data from the *Euclid* mission of the European Space Agency (ESA), 2024, `https://doi.org/10.57780/esa-qmocze3`. The Euclid Consortium acknowledges the European Space Agency and a number of agencies and institutes that have supported the development of *Euclid*, in particular the Agenzia Spaziale Italiana, the Austrian Forschungsförderungsgesellschaft, funded through BMK, the Belgian Science Policy, the Canadian Euclid Consortium, the Deutsches Zentrum für Luft- und Raumfahrt, the DTU Space and the Niels Bohr Institute in Denmark, the French Centre National d'Etudes Spatiales, the Fundação para a Ciência e a Tecnologia, the Hungarian Academy of Sciences, the Ministerio de Ciencia, Innovación y Universidades, the National Aeronautics and Space Administration, the National Astronomical Observatory of Japan, the Netherlandse Onderzoekschool Voor Astronomie, the Norwegian Space Agency, the Research Council of Finland, the Romanian Space Agency, the State Secretariat for Education, Research, and Innovation (SERI) at the Swiss Space Office (SSO), and the United Kingdom Space Agency. A complete and detailed list is available on the *Euclid* web site (`http://www.euclid-ec.org`). This work made use of Astropy[5]: a community-developed core Python package and an ecosystem of tools and resources for astronomy (Astropy Collaboration 2013; Astropy Collaboration 2018, 2022) and Matplotlib (Hunter 2007). This research has made use of Aladin sky atlas, CDS, Strasbourg Astronomical Observatory, France (Bonnarel et al. 2000).

References

Abbott, T. M. C., Adamów, M., Aguena, M., et al. 2021, ApJS, 255, 20
Abell, G. O., Corwin, Harold G., J., & Olowin, R. P. 1989, ApJS, 70, 1
Adams, N. J., Conselice, C. J., Ferreira, L., et al. 2023, MNRAS, 518, 4755
Alonso Asensio, I., Dalla Vecchia, C., Bahé, Y. M., Barnes, D. J., & Kay, S. T. 2020, MNRAS, 494, 1859
Applegate, D. E., von der Linden, A., Kelly, P. L., et al. 2014, MNRAS, 439, 48
Astropy Collaboration (Robitaille, T. P., et al.) 2013, A&A, 558, A33
Astropy Collaboration (Price-Whelan, A. M., et al.) 2018, AJ, 156, 123
Astropy Collaboration (Price-Whelan, A. M., et al.) 2022, ApJ, 935, 167
Atek, H., Chemerynska, I., Wang, B., et al. 2023, MNRAS, 524, 5486
Barbary, K. 2016, J. Open Source Softw., 1, 58
Bartelmann, M., & Schneider, P. 2001, Phys. Rep., 340, 291
Bertin, E. 2011, in Astronomical Society of the Pacific Conference Series, 442, Astronomical Data Analysis Software and Systems XX, eds. I. N. Evans, A. Accomazzi, D. J. Mink, & A. H. Rots, 435
Bertin, E., & Arnouts, S. 1996, A&AS, 117, 393
Bertin, E., Mellier, Y., Radovich, M., et al. 2002, in Astronomical Society of the Pacific Conference Series, 281, Astronomical Data Analysis Software and Systems XI, eds. D. A. Bohlender, D. Durand, & T. H. Handley, 228
Bertin, E., Schefer, M., Apostolakos, N., et al. 2022, SourceXtractor++: Extracts sources from astronomical images, Astrophysics Source Code Library: [`record ascl:2212.018`]
Bleem, L. E., Stalder, B., de Haan, T., et al. 2015, ApJS, 216, 27
Bleem, L. E., Klein, M., Abbot, T. M. C., et al. 2024, Open J. Astrophys., 7, 13
Boehringer, H., Tanaka, Y., Mushotzky, R. F., Ikebe, Y., & Hattori, M. 1998, A&A, 334, 789
Bonnarel, F., Fernique, P., Bienaymé, O., et al. 2000, A&AS, 143, 33
Bouwens, R. J., Illingworth, G. D., Oesch, P. A., et al. 2015, ApJ, 803, 34
Bowler, R. A. A., Dunlop, J. S., McLure, R. J., & McLeod, D. J. 2017, MNRAS, 466, 3612
Bowler, R. A. A., Jarvis, M. J., Dunlop, J. S., et al. 2020, MNRAS, 493, 2059
Brammer, G. B., van Dokkum, P. G., & Coppi, P. 2008, ApJ, 686, 1503
Brammer, G., Strait, V., Matharu, J., & Momcheva, I. 2022, `https://doi.org/10.5281/zenodo.6672538`
Bulbul, E., Liu, A., Kluge, M., et al. 2024, A&A, 685, A106
Chemerynska, I., Atek, H., Furtak, L. J., et al. 2024, MNRAS, 531, 2615
Contini, E. 2021, Galaxies, 9, 60
Contreras-Santos, A., Knebe, A., Cui, W., et al. 2024, A&A, 683, A59
Cowie, L. L., Barger, A. J., Bauer, F. E., et al. 2022, ApJ, 939, 5
Cuillandre, J.-C., Bertin, E., Bolzonella, M., et al. 2025, A&A, 697, A6 (*Euclid* on Sky SI)
Dark Energy Survey Collaboration, Abbott, T., Abdalla, F. B., et al. 2016, MNRAS, 460, 1270

---

[5] `http://www.astropy.org`

Deason, A. J., Oman, K. A., Fattahi, A., et al. 2021, MNRAS, 500, 4181
Dey, A., Schlegel, D. J., Lang, D., et al. 2019, AJ, 157, 168
Diego, J. M., Tegmark, M., Protopapas, P., & Sandvik, H. B. 2007, MNRAS, 375, 958
Diehl, H. T., Buckley-Geer, E. J., Lindgren, K. A., et al. 2017, ApJS, 232, 15
Donnan, C. T., McLure, R. J., Dunlop, J. S., et al. 2024, MNRAS, submitted, [arXiv:2403.03171]
Erben, T., Van Waerbeke, L., Bertin, E., Mellier, Y., & Schneider, P. 2001, A&A, 366, 717
Euclid Collaboration (Barnett, R., et al.) 2019, A&A, 631, A85
Euclid Collaboration (Martinet, N., et al.) 2019, A&A, 627, A59
Euclid Collaboration (Scaramella, R., et al.) 2022, A&A, 662, A112
Euclid Collaboration (van Mierlo, S. E., et al.) 2022, A&A, 666, A200
Euclid Collaboration (Bretonnière), H., et al.) 2023, A&A, 671, A102
Euclid Collaboration (Merlin, E., et al.) 2023, A&A, 671, A101
Euclid Collaboration (Cropper, M. S., et al.) 2025, A&A, 697, A2 (*Euclid* on Sky SI)
Euclid Collaboration (Jahnke, K., et al.) 2025, A&A, 697, A3 (*Euclid* on Sky SI)
Euclid Collaboration (Mellier, Y., et al.) 2025, A&A, 697, A1 (*Euclid* on Sky SI)
Everett, W. B., Zhang, L., Crawford, T. M., et al. 2020, ApJ, 900, 55
Feix, M., Zhao, H., Fedeli, C., Pestaña, J. L. G., & Hoekstra, H. 2010, Phys. Rev. D, 82, 124003
Feldmeier, J. J., Mihos, J. C., Morrison, H. L., et al. 2004, ApJ, 609, 617
Finkelstein, S. L., Ryan, Jr., R. E., Papovich, C., et al. 2015, ApJ, 810, 71
Fitzpatrick, E. L., & Massa, D. 2007, ApJ, 663, 320
Flaugher, B. 2005, Int. J. Mod. Phys. A, 20, 3121
Flaugher, B., Diehl, H. T., Honscheid, K., et al. 2015, AJ, 150, 150
Golden-Marx, J. B., Zhang, Y., Ogando, R. L. C., et al. 2023, MNRAS, 521, 478
Gonzalez, A. H., Gettings, D. P., Brodwin, M., et al. 2019, ApJS, 240, 33
Gonzalez, A. H., George, T., Connor, T., et al. 2021, MNRAS, 507, 963
Harikane, Y., Ouchi, M., Oguri, M., et al. 2023, ApJS, 265, 5
Hernández-Martín, B., Schrabback, T., Hoekstra, H., et al. 2020, A&A, 640, A117
Hilton, M., Sifón, C., Naess, S., et al. 2021, ApJS, 253, 3
Hoekstra, H., Franx, M., Kuijken, K., & Squires, G. 1998, ApJ, 504, 636
Hunter, J. D. 2007, Comput. Sci. Eng., 9, 90
Kaiser, N., Squires, G., & Broadhurst, T. 1995, ApJ, 449, 460
Katgert, P., Mazure, A., Perea, J., et al. 1996, A&A, 310, 8
Kluge, M., Neureiter, B., Riffeser, A., et al. 2020, ApJS, 247, 43
Kluge, M., Hatch, N. A., Montes, M., et al. 2025, A&A, 697, A13 (*Euclid* on Sky SI)
Koekemoer, A. M., Faber, S. M., Ferguson, H. C., et al. 2011, ApJS, 197, 36
Kümmel, M., Álvarez-Ayllón, A., Bertin, E., et al. 2022, arXiv e-prints [arXiv:2212.02428]
Le Borgne, J. F., Mathez, G., Mellier, Y., et al. 1991, A&AS, 88, 133
Liu, Q., Yee, H. K. C., Drissen, L., et al. 2021, ApJ, 908, 228
Luppino, G. A., & Kaiser, N. 1997, ApJ, 475, 20
Mandelbaum, R., Rowe, B., Armstrong, R., et al. 2015, MNRAS, 450, 2963
McInnes, R. N., Menanteau, F., Heavens, A. F., et al. 2009, MNRAS, 399, L84
Merloni, A., Lamer, G., Liu, T., et al. 2024, A&A, 682, A34
Miyazaki, S., Komiyama, Y., Sekiguchi, M., et al. 2002, PASJ, 54, 833
Montes, M. 2022, Nat. Astron., 6, 308
Montes, M., & Trujillo, I. 2019, MNRAS, 482, 2838
Murante, G., Giovalli, M., Gerhard, O., et al. 2007, MNRAS, 377, 2
Navarro, J. F., Frenk, C. S., & White, S. D. M. 1996, ApJ, 462, 563
Okabe, N., & Smith, G. P. 2016, MNRAS, 461, 3794
Olmstead, A., Rigby, J. R., Swinbank, M., & Veilleux, S. 2014, AJ, 148, 65
Ota, K., Richard, J., Iye, M., et al. 2012, MNRAS, 423, 2829
Ouchi, M., Shimasaku, K., Okamura, S., et al. 2004, ApJ, 611, 685
Pello, R., Le Borgne, J.-F., Soucail, G., Mellier, Y., & Sanahuja, B. 1991, ApJ, 366, 405
Planck Collaboration XIII. 2016, A&A, 594, A13
Planck Collaboration Int. XLVII. 2016, A&A, 596, A108
Richard, J., Claeyssens, A., Lagattuta, D., et al. 2021, A&A, 646, A83
Schneider, P., & Er, X. 2008, A&A, 485, 363
Schrabback, T., Applegate, D., Dietrich, J. P., et al. 2018, MNRAS, 474, 2635
Schrabback, T., Bocquet, S., Sommer, M., et al. 2021, MNRAS, 505, 3923
Sendra, I., Diego, J. M., Broadhurst, T., & Lazkoz, R. 2014, MNRAS, 437, 2642
Sereno, M., & Ettori, S. 2017, MNRAS, 468, 3322
Simon, P., Taylor, A. N., & Hartlap, J. 2009, MNRAS, 399, 48
Sohn, J., Fabricant, D. G., Geller, M. J., Hwang, H. S., & Diaferio, A. 2020, ApJ, 902, 17
Sunyaev, R. A., & Zeldovich, Y. B. 1972a, A&A, 20, 189
Sunyaev, R. A., & Zeldovich, Y. B. 1972b, Comments Astrophys. Space Phys., 4, 173
Sunyaev, R. A., & Zeldovich, I. B. 1980, ARA&A, 18, 537
von der Linden, A., Allen, M. T., Applegate, D. E., et al. 2014, MNRAS, 439, 2
Weaver, J. R., Taamoli, S., McPartland, C. J. R., et al. 2025, A&A, 697, A16 (*Euclid* on Sky SI)
Yagi, M., Kashikawa, N., Sekiguchi, M., et al. 2002, AJ, 123, 66
Yoo, J., Ko, J., Sabiu, C. G., et al. 2022, ApJS, 261, 28
Zohren, H., Schrabback, T., Bocquet, S., et al. 2022, A&A, 668, A18

---

[1] Institut d'Astrophysique de Paris, UMR 7095, CNRS, and Sorbonne Université, 98 bis boulevard Arago, 75014 Paris, France
[2] Aix-Marseille Université, CNRS, CNES, LAM, Marseille, France
[3] Department of Astronomy, University of Massachusetts, Amherst, MA 01003, USA
[4] Instituto de Física de Cantabria, Edificio Juan Jordá, Avenida de los Castros, 39005 Santander, Spain
[5] Universität Innsbruck, Institut für Astro- und Teilchenphysik, Technikerstr. 25/8, 6020 Innsbruck, Austria
[6] School of Physics and Astronomy, University of Nottingham, University Park, Nottingham NG7 2RD, UK
[7] Université Paris-Saclay, CNRS, Institut d'astrophysique spatiale, 91405 Orsay, France
[8] Department of Astronomy, University of Geneva, ch. d'Ecogia 16, 1290 Versoix, Switzerland
[9] Physics and Astronomy Department, University of California, 900 University Ave., Riverside, CA 92521, USA
[10] Institute for Astronomy, University of Edinburgh, Royal Observatory, Blackford Hill, Edinburgh EH9 3HJ, UK
[11] Instituto de Astrofísica de Andalucía, CSIC, Glorieta de la Astronomía, 18080, Granada, Spain
[12] Observatorio Nacional, Rua General Jose Cristino, 77-Bairro Imperial de Sao Cristovao, Rio de Janeiro 20921-400, Brazil
[13] Université Paris-Saclay, Université Paris Cité, CEA, CNRS, AIM, 91191 Gif-sur-Yvette, France
[14] Max-Planck-Institut für Astronomie, Königstuhl 17, 69117 Heidelberg, Germany
[15] INAF-Osservatorio di Astrofisica e Scienza dello Spazio di Bologna, Via Piero Gobetti 93/3, 40129 Bologna, Italy
[16] Jodrell Bank Centre for Astrophysics, Department of Physics and Astronomy, University of Manchester, Oxford Road, Manchester M13 9PL, UK
[17] The University of Texas at Austin, Austin, TX 78712, USA
[18] Department of Physics, Centre for Extragalactic Astronomy, Durham University, South Road DH1 3LE, UK
[19] Department of Physics, Institute for Computational Cosmology, Durham University, South Road DH1 3LE, UK
[20] Astrophysics Research Centre, University of KwaZulu-Natal, Westville Campus, Durban 4041, South Africa
[21] School of Mathematics, Statistics & Computer Science, University of KwaZulu-Natal, Westville Campus, Durban 4041, South Africa
[22] STAR Institute, Quartier Agora – Allée du six Août, 19c 4000 Liège, Belgium
[23] Centre de Recherche Astrophysique de Lyon, UMR5574, CNRS, Université Claude Bernard Lyon 1, ENS de Lyon, 69230 Saint-Genis-Laval, France
[24] School of Physical Sciences, The Open University, Milton Keynes MK7 6AA, UK
[25] Niels Bohr Institute, University of Copenhagen, Jagtvej 128, 2200 Copenhagen, Denmark
[26] Dipartimento di Fisica "Aldo Pontremoli", Università degli Studi di Milano, Via Celoria 16, 20133 Milano, Italy
[27] INAF – Osservatorio Astronomico di Trieste, Via G. B. Tiepolo 11, 34143 Trieste, Italy
[28] IFPU, Institute for Fundamental Physics of the Universe, via Beirut 2, 34151 Trieste, Italy
[29] INAF – Osservatorio Astronomico di Roma, Via Frascati 33, 00078 Monteporzio Catone, Italy
[30] INAF-IASF Milano, Via Alfonso Corti 12, 20133 Milano, Italy
[31] Astrophysics Group, Blackett Laboratory, Imperial College London, London SW7 2AZ, UK
[32] Institute of Physics, Laboratory of Astrophysics, Ecole Polytechnique Fédérale de Lausanne (EPFL), Observatoire de Sauverny, 1290 Versoix, Switzerland

[33] Institut d'Astrophysique de Paris, 98bis Boulevard Arago, 75014 Paris, France
[34] Cosmic Dawn Center (DAWN), Denmark
[35] INFN-Sezione di Bologna, Viale Berti Pichat 6/2, 40127 Bologna, Italy
[36] Kobayashi-Maskawa Institute for the Origin of Particles and the Universe, Nagoya University, Chikusa-ku, Nagoya 464-8602, Japan
[37] Institute for Advanced Research, Nagoya University, Chikusa-ku, Nagoya 464-8601, Japan
[38] Kavli Institute for the Physics and Mathematics of the Universe (WPI), University of Tokyo, Kashiwa, Chiba 277-8583, Japan
[39] Instituto de Astrofísica de Canarias, Calle Vía Láctea s/n, 38204 San Cristóbal de La Laguna, Tenerife, Spain
[40] Departamento de Astrofísica, Universidad de La Laguna, 38206, La Laguna, Tenerife, Spain
[41] Department of Mathematics, Imperial College London, London SW7 2AZ, UK
[42] Physics Program, Graduate School of Advanced Science and Engineering, Hiroshima University, 1-3-1 Kagamiyama, Higashi-Hiroshima, Hiroshima 739-8526, Japan
[43] Hiroshima Astrophysical Science Center, Hiroshima University, 1-3-1 Kagamiyama, Higashi-Hiroshima, Hiroshima 739-8526, Japan
[44] Core Research for Energetic Universe, Hiroshima University, 1-3-1, Kagamiyama, Higashi-Hiroshima, Hiroshima 739-8526, Japan
[45] Dipartimento di Fisica e Scienze della Terra, Università degli Studi di Ferrara, Via Giuseppe Saragat 1, 44122 Ferrara, Italy
[46] Universitäts-Sternwarte München, Fakultät für Physik, Ludwig-Maximilians-Universität München, Scheinerstrasse 1, 81679 München, Germany
[47] Max Planck Institute for Extraterrestrial Physics, Giessenbachstr. 1, 85748 Garching, Germany
[48] European Spae Agency/ESTEC, Keplerlaan 1, 2201 AZ Noordwijk, The Netherlands
[49] Observatoire Astronomique de Strasbourg (ObAS), Université de Strasbourg – CNRS, UMR 7550, Strasbourg, France
[50] Kapteyn Astronomical Institute, University of Groningen, PO Box 800, 9700 AV Groningen, The Netherlands
[51] Department of Physics, Université de Montréal, 2900 Edouard Montpetit Blvd, Montréal, Québec H3T 1J4, Canada
[52] Aurora Technology for European Space Agency (ESA), Camino bajo del Castillo, s/n, Urbanizacion Villafranca del Castillo, Villanueva de la Cañada, 28692 Madrid, Spain
[53] ESAC/ESA, Camino Bajo del Castillo, s/n., Urb. Villafranca del Castillo, 28692 Villanueva de la Cañada, Madrid, Spain
[54] School of Mathematics and Physics, University of Surrey, Guildford, Surrey GU2 7XH, UK
[55] INAF – Osservatorio Astronomico di Brera, Via Brera 28, 20122 Milano, Italy
[56] Dipartimento di Fisica e Astronomia, Università di Bologna, Via Gobetti 93/2, 40129 Bologna, Italy
[57] INAF – Osservatorio Astronomico di Padova, Via dell'Osservatorio 5, 35122 Padova, Italy
[58] Centre National d'Etudes Spatiales – Centre spatial de Toulouse, 18 avenue Edouard Belin, 31401 Toulouse Cedex 9, France
[59] INAF – Osservatorio Astrofisico di Torino, Via Osservatorio 20, 10025 Pino Torinese (TO), Italy
[60] Dipartimento di Fisica, Università di Genova, Via Dodecaneso 33, 16146, Genova, Italy
[61] INFN – Sezione di Genova, Via Dodecaneso 33, 16146, Genova, Italy
[62] Department of Physics "E. Pancini", University Federico II, Via Cinthia 6, 80126 Napoli, Italy
[63] INAF – Osservatorio Astronomico di Capodimonte, Via Moiariello 16, 80131 Napoli, Italy
[64] INFN section of Naples, Via Cinthia 6, 80126 Napoli, Italy
[65] Instituto de Astrofísica e Ciências do Espaço, Universidade do Porto, CAUP, Rua das Estrelas, 4150-762 Porto, Portugal
[66] Faculdade de Ciências da Universidade do Porto, Rua do Campo de Alegre, 4150-007 Porto, Portugal
[67] Dipartimento di Fisica, Università degli Studi di Torino, Via P. Giuria 1, 10125 Torino, Italy
[68] INFN – Sezione di Torino, Via P. Giuria 1, 10125 Torino, Italy
[69] Mullard Space Science Laboratory, University College London, Holmbury St Mary, Dorking, Surrey RH5 6NT, UK
[70] INFN – Sezione di Roma, Piazzale Aldo Moro 2, c/o Dipartimento di Fisica, Edificio G. Marconi, 00185 Roma, Italy
[71] Centro de Investigaciones Energéticas, Medioambientales y Tecnológicas (CIEMAT), Avenida Complutense 40, 28040 Madrid, Spain
[72] Port d'Informació Científica, Campus UAB, C. Albareda s/n, 08193 Bellaterra (Barcelona), Spain
[73] Institute for Theoretical Particle Physics and Cosmology (TTK), RWTH Aachen University, 52056 Aachen, Germany
[74] Institute of Space Sciences (ICE, CSIC), Campus UAB, Carrer de Can Magrans, s/n, 08193 Barcelona, Spain
[75] Institut d'Estudis Espacials de Catalunya (IEEC), Edifici RDIT, Campus UPC, 08860 Castelldefels, Barcelona, Spain
[76] Dipartimento di Fisica e Astronomia "Augusto Righi" – Alma Mater Studiorum Università di Bologna, Viale Berti Pichat 6/2, 40127 Bologna, Italy
[77] European Space Agency/ESRIN, Largo Galileo Galilei 1, 00044 Frascati, Roma, Italy
[78] Université Claude Bernard Lyon 1, CNRS/IN2P3, IP2I Lyon, UMR 5822, Villeurbanne, 69100, France
[79] UCB Lyon 1, CNRS/IN2P3, IUF, IP2I Lyon, 4 rue Enrico Fermi, 69622 Villeurbanne, France
[80] Departamento de Física, Faculdade de Ciências, Universidade de Lisboa, Edifício C8, Campo Grande, 1749-016 Lisboa, Portugal
[81] Instituto de Astrofísica e Ciências do Espaço, Faculdade de Ciências, Universidade de Lisboa, Campo Grande, 1749-016 Lisboa, Portugal
[82] INAF – Istituto di Astrofisica e Planetologia Spaziali, via del Fosso del Cavaliere, 100, 00100 Roma, Italy
[83] INFN – Padova, Via Marzolo 8, 35131 Padova, Italy
[84] School of Physics, HH Wills Physics Laboratory, University of Bristol, Tyndall Avenue, Bristol, BS8 1TL, UK
[85] Aix-Marseille Université, CNRS/IN2P3, CPPM, Marseille, France
[86] Istituto Nazionale di Fisica Nucleare, Sezione di Bologna, Via Irnerio 46, 40126 Bologna, Italy
[87] FRACTAL S.L.N.E., calle Tulipán 2, Portal 13 1A, 28231, Las Rozas de Madrid, Spain
[88] Institute of Theoretical Astrophysics, University of Oslo, PO Box 1029 Blindern, 0315 Oslo, Norway
[89] Leiden Observatory, Leiden University, Einsteinweg 55, 2333 CC Leiden, The Netherlands
[90] Jet Propulsion Laboratory, California Institute of Technology, 4800 Oak Grove Drive, Pasadena, CA 91109, USA
[91] Department of Physics, Lancaster University, Lancaster LA1 4YB, UK
[92] Felix Hormuth Engineering, Goethestr. 17, 69181 Leimen, Germany
[93] Technical University of Denmark, Elektrovej 327, 2800 Kgs. Lyngby, Denmark
[94] NASA Goddard Space Flight Center, Greenbelt, MD 20771, USA
[95] Department of Physics and Helsinki Institute of Physics, Gustaf Hällströmin katu 2, 00014 University of Helsinki, Finland
[96] Université de Genève, Département de Physique Théorique and Centre for Astroparticle Physics, 24 quai Ernest-Ansermet, 1211 Genève 4, Switzerland
[97] Department of Physics, PO Box 64, 00014 University of Helsinki, Finland
[98] Helsinki Institute of Physics, Gustaf Hällströmin katu 2, University of Helsinki, Helsinki, Finland
[99] Department of Physics and Astronomy, University College London, Gower Street, London WC1E 6BT, UK
[100] NOVA optical infrared instrumentation group at ASTRON, Oude Hoogeveensedijk 4, 7991PD, Dwingeloo, The Netherlands
[101] INFN-Sezione di Milano, Via Celoria 16, 20133 Milano, Italy
[102] Universität Bonn, Argelander-Institut für Astronomie, Auf dem Hügel 71, 53121 Bonn, Germany

[103] Dipartimento di Fisica e Astronomia "Augusto Righi" – Alma Mater Studiorum Università di Bologna, via Piero Gobetti 93/2, 40129 Bologna, Italy
[104] Université Côte d'Azur, Observatoire de la Côte d'Azur, CNRS, Laboratoire Lagrange, Bd de l'Observatoire, CS 34229, 06304 Nice cedex 4, France
[105] Université Paris Cité, CNRS, Astroparticule et Cosmologie, 75013 Paris, France
[106] Institut de Física d'Altes Energies (IFAE), The Barcelona Institute of Science and Technology, Campus UAB, 08193 Bellaterra (Barcelona), Spain
[107] Department of Physics and Astronomy, University of Aarhus, Ny Munkegade 120, 8000 Aarhus C, Denmark
[108] Waterloo Centre for Astrophysics, University of Waterloo, Waterloo, Ontario N2L 3G1, Canada
[109] Department of Physics and Astronomy, University of Waterloo, Waterloo, Ontario N2L 3G1, Canada
[110] Perimeter Institute for Theoretical Physics, Waterloo, Ontario N2L 2Y5, Canada
[111] Space Science Data Center, Italian Space Agency, via del Politecnico snc, 00133 Roma, Italy
[112] Institute of Space Science, Str. Atomistilor, nr. 409 Măgurele, Ilfov, 077125, Romania
[113] Dipartimento di Fisica e Astronomia "G. Galilei", Università di Padova, Via Marzolo 8, 35131 Padova, Italy
[114] Departamento de Física, FCFM, Universidad de Chile, Blanco Encalada 2008, Santiago, Chile
[115] Satlantis, University Science Park, Sede Bld 48940, Leioa-Bilbao, Spain
[116] Centre for Electronic Imaging, Open University, Walton Hall, Milton Keynes MK7 6AA, UK
[117] Infrared Processing and Analysis Center, California Institute of Technology, Pasadena, CA 91125, USA
[118] Instituto de Astrofísica e Ciências do Espaço, Faculdade de Ciências, Universidade de Lisboa, Tapada da Ajuda, 1349-018 Lisboa, Portugal
[119] Universidad Politécnica de Cartagena, Departamento de Electrónica y Tecnología de Computadoras, Plaza del Hospital 1, 30202 Cartagena, Spain
[120] Institut de Recherche en Astrophysique et Planétologie (IRAP), Université de Toulouse, CNRS, UPS, CNES, 14 Av. Edouard Belin, 31400 Toulouse, France
[121] INFN-Bologna, Via Irnerio 46, 40126 Bologna, Italy
[122] Dipartimento di Fisica, Università degli studi di Genova, and INFN-Sezione di Genova, via Dodecaneso 33, 16146, Genova, Italy
[123] INFN, Sezione di Trieste, Via Valerio 2, 34127 Trieste TS, Italy
[124] SISSA, International School for Advanced Studies, Via Bonomea 265, 34136 Trieste TS, Italy
[125] INAF, Istituto di Radioastronomia, Via Piero Gobetti 101, 40129 Bologna, Italy
[126] Institut für Theoretische Physik, University of Heidelberg, Philosophenweg 16, 69120 Heidelberg, Germany
[127] Université St Joseph; Faculty of Sciences, Beirut, Lebanon
[128] Junia, EPA department, 41 Bd Vauban, 59800 Lille, France
[129] ICSC – Centro Nazionale di Ricerca in High Performance Computing, Big Data e Quantum Computing, Via Magnanelli 2, Bologna, Italy
[130] Department of Physics and Astronomy, University of British Columbia, Vancouver, BC V6T 1Z1, Canada